

Single-Cell Phenotyping within Transparent Intact Tissue through Whole-Body Clearing

Bin Yang,¹ Jennifer B. Treweek,¹ Rajan P. Kulkarni,^{1,2} Benjamin E. Deverman,¹ Chun-Kan Chen,¹ Eric Lubeck,¹ Sheel Shah,¹ Long Cai,³ and Viviana Gradinaru^{1,*}

¹Division of Biology and Biological Engineering, California Institute of Technology, Pasadena, CA 91125, USA

²Division of Dermatology, Department of Medicine, David Geffen School of Medicine at UCLA, Los Angeles, CA 90095, USA

³Division of Chemistry and Chemical Engineering, California Institute of Technology, Pasadena, CA 91125, USA

*Correspondence: viviana@caltech.edu

<http://dx.doi.org/10.1016/j.cell.2014.07.017>

SUMMARY

Understanding the structure-function relationships at cellular, circuit, and organ-wide scale requires 3D anatomical and phenotypical maps, currently unavailable for many organs across species. At the root of this knowledge gap is the absence of a method that enables whole-organ imaging. Herein, we present techniques for tissue clearing in which whole organs and bodies are rendered macromolecule-permeable and optically transparent, thereby exposing their cellular structure with intact connectivity. We describe PACT (*passive clarity technique*), a protocol for passive tissue clearing and immunostaining of intact organs; RIMS (*refractive index matching solution*), a mounting media for imaging thick tissue; and PARS (*perfusion-assisted agent release in situ*), a method for whole-body clearing and immunolabeling. We show that in rodents PACT, RIMS, and PARS are compatible with endogenous-fluorescence, immunohistochemistry, RNA single-molecule FISH, long-term storage, and microscopy with cellular and subcellular resolution. These methods are applicable for high-resolution, high-content mapping and phenotyping of normal and pathological elements within intact organs and bodies.

INTRODUCTION

Facile and physiologically informative optical access to intact tissues has long been a goal of biologists. As early as the 1800s, work by scientists such as Werner Spalteholz revealed the utility of rendering tissue optically transparent for anatomical and biomedical studies (Spalteholz, 1914). Although the Spalteholz technique and its variants incur damage to tissue integrity and morphology, they are still in use a century later (Steinke and Wolff, 2001), highlighting barriers to the adoption

of more recent tissue-clearing methods and modern microscopy techniques. While separate tissue-clearing protocols have strengths in an application-specific context, none is able to fully surmount the most common obstacles: unconfirmed generalizability across organs other than the brain or embryo, difficulties in execution, and incompatibility with endogenous fluorescence and/or post hoc immunohistochemistry (Table S1). Thus motivation to improve tissue-clearing protocols is sustained around three main objectives: (1) efficient clearing of both central organs and peripheral tissue (2) preservation of cellular and subcellular structures of multiple organ types; and (3) compatibility with endogenous fluorescent protein expression and post hoc detection of DNA, RNA, and peptides.

The payoffs of such a method are optical access throughout large volumes of tissues, enabling the study of cell-to-cell spatial relationships and long-range neural connectivity in the context of preserved tissue morphology (Chung and Deisseroth, 2013; Chung et al., 2013; Kim et al., 2013; Zhang et al., 2014). In conjunction with fluorescent tracers, tissue clearing facilitates the identification of interacting cellular structures, including diverging or converging nerves and vasculature at their target sites throughout the body. Fine-scale subcellular analysis of cleared specimens using standard protein and nucleic acid probes should also be achievable in the context of cleared tissues.

We have developed a methodology for whole-organism clearing, building upon previous techniques such as CLARITY, SCALE, SeeDB, ClearT, 3DISCO, CUBIC, dibenzyl ether (DBE), and BABB (Murray's Clear) (Becker et al., 2012; Chung et al., 2013; Dodt et al., 2007; Ertürk et al., 2012a; Hama et al., 2011; Ke et al., 2013; Kuwajima et al., 2013; Susaki et al., 2014). Each of these has made a clear contribution: hydrogel embedding to stabilize tissue structures (Chung et al., 2013), fluorescent protein-compatible clearing reagents (Susaki et al., 2014), and imaging approaches for large or challenging tissue samples (Becker et al., 2013; Tseng et al., 2009; Tomer et al., 2014). Although a comprehensive discussion of their respective strengths and weaknesses is beyond the scope of this text, a few critical points merit mention. First, in the original proof of principle for each of these techniques, the detailed

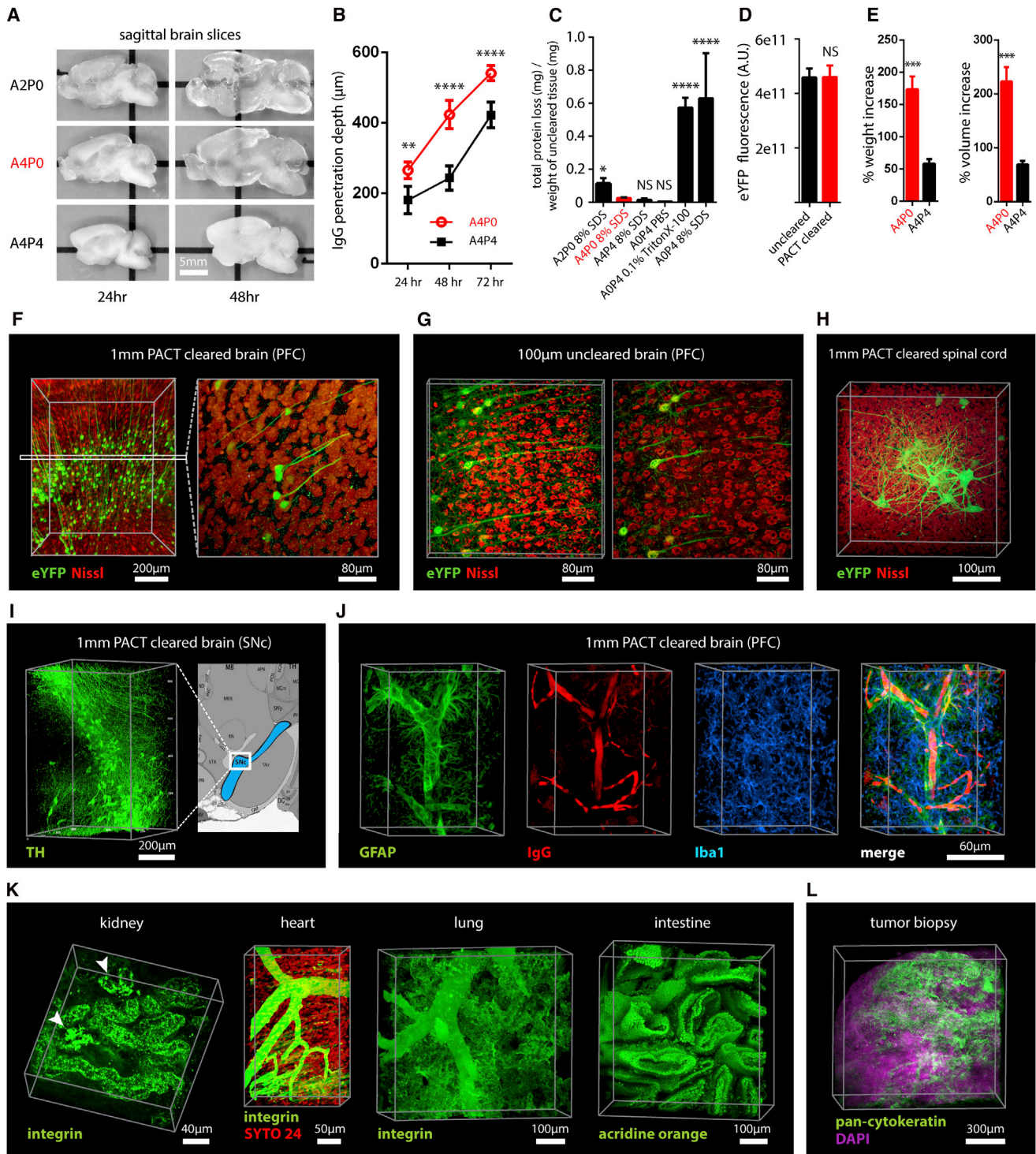


Figure 1. PACT Clearing of A4P0 Tissue-Hydrogel Hybrid Achieves Optimal Transparency and Immunohistochemistry Compatibility across Organs

(A) Optical transparency comparison of 3 mm adult mouse sagittal blocks of A2P0, A4P0, and A4P4 tissue-hydrogel hybrid cleared for 24 hr and 48 hr.

(B) Compared to A4P4, A4P0 tissue-hydrogel hybrid showed faster antibody penetration (n = 6 fields of view per sample).

(C) The percentage of protein loss from 1 mm mouse brain slices (n = 6 slices for each clearing condition); statistical significance is shown for each condition versus A4P0 8% SDS (red).

(D) The integrated eYFP fluorescence intensity in arbitrary units (A.U.) of uncleared and cleared 1 mm Thy1-eYFP mouse brain slices (n = 6 slices).

(E) Compared to A4P4, the A4P0 hydrogel-tissue hybrid showed higher tissue expansion and weight gain postclearing.

(legend continued on next page)

methods and optimized protocols were only presented for clearing brain tissue, and occasionally for the spinal cord (Ertürk et al., 2012a; Zhang et al., 2014) or whole embryo (Dodt et al., 2007; Hama et al., 2011). 3DISCO represents, to date, the most complete elucidation of a clearing method across different tissues. However, as is the case with many prior clearing protocols (Table S1 available online), 3DISCO's clearing reagents (tetrahydrofuran and DBE) substantially quench fluorescent signals in tissue samples (Ertürk et al., 2012a). CLARITY (Chung et al., 2013) and CUBIC (Susaki et al., 2014) bypass the fluorescence quenching problem, but CLARITY in its original form used electrophoretic tissue clearing (ETC) to extract lipids from large samples, which can be challenging to implement and can cause variability in final tissue quality, including epitope loss, damage to fine processes, and tissue browning due to heating (forum.claritytechniques.org). This has led to variations of CLARITY using passive lipid extraction (Zhang et al., 2014, with protocol described in detail in Tomer et al., 2014, along with thermal acceleration of clearing and improved imaging). CUBIC also achieves tissue transparency by passively clearing phospholipids and is compatible with hydrogel embedding. The main weakness of passive clearing methods is their slow speed, which makes them unsuited for clearing large tissue volumes or whole organisms.

Herein, we propose a methodology to facilitate fast, whole-brain and whole-body clearing using systemic or cerebrospinal circulation to directly deliver clarifying agents. A first step was to optimize the hydrogel embedding, clearing, and imaging reagents, which resulted in PACT, for *passive clarity technique*, for quicker passive lipid extraction of 1- to 3-mm-thick tissues. To image PACT-cleared tissue we have developed a *refractive index matching solution* (RIMS)—a custom economical recipe, with outcome similar to FocusClear (Chung et al., 2013; Moy et al., 2013; Tseng et al., 2009). The PACT reagents may be delivered either intracranially or via the vasculature to achieve whole-brain and -body clearing and labeling. We term the latter PARS, for *perfusion-assisted agent release in situ*. All steps for PARS, including preservation, clearing, and labeling, are performed in situ prior to tissue extraction. We demonstrate below that PARS, together with RIMS, transform opaque, intact, whole-organisms into optically transparent, fluorescently labeled samples for visualization with conventional confocal microscopy and phenotypic analysis at the cellular, subcellular, and even single-molecule transcripts level.

RESULTS

Optimized Method for Passive Clearing and Immunostaining of Whole Organs in the Rodent

Similar to the CLARITY method (Chung et al., 2013; Tomer et al., 2014), we render thick tissue optically transparent for imaging in three main steps. First, tissue is crosslinked and hybridized to hydrogel monomers to stabilize biomacromolecules. Second, tissue lipids are extracted from the tissue-hydrogel matrix with ionic detergents. Third, cleared tissue is embedded in RIMS for imaging, or for long-term storage. Although whole-body clearing was our primary goal, we recognized that the processing of small or particularly fragile specimens and organs would best be accomplished by a mild, passive clearing protocol. We developed PACT for rendering rodent whole organs, their 1- to 3-mm-thick sections, including brain, spinal cord, kidney, heart, lung, and intestine, or human tissue biopsies transparent. The clearing speed depends in part on the rate of lipid solvation by detergent micelles, and the rate of diffusion of detergent micelles in tissue (Hoffman, 2002). However, unless an applied force accelerates their diffusion through tissue, such as the electric field in CLARITY's ETC (Chung et al., 2013; Tomer et al., 2014), lipid extraction by large micelles is slow. We tested different detergents at various concentrations for their ability to passively clear 3 mm coronal mouse brain blocks over a 3 day incubation. Sodium dodecyl sulfate (SDS) at all concentrations was superior for lipid solvation and removal from brain tissue to other detergents, and moreover, only the 8% SDS concentration achieved uniform clearing throughout the entire 3 mm block (Figure S1A).

We hypothesized that a decrease in the crosslink density of the tissue-hydrogel would facilitate both lipid extraction and macromolecule penetration into thick, highly myelinated or fibrous tissue during subsequent immunohistochemistry. To test this, 3 mm brain sections were infused with varying combinations and concentrations of formaldehyde, acrylamide, and bis-acrylamide, degassed, and polymerized at 37°C. The efficiency of tissue clearing (Figure 1A) and the depth of antibody penetration (Figure 1B) increased significantly when lower concentrations of formaldehyde and acrylamide were used and when bis-acrylamide, an acrylamide crosslinking agent used in CLARITY (Tomer et al., 2014), was excluded from the cocktail of hydrogel monomers. Upon observing a qualitative increase in tissue transparency in the tissue-hydrogels prepared with lower acrylamide concentrations (Figure 1A), we assayed the different PACT tissue preparations for protein loss, tissue

(F–H) Thy1-eYFP mouse sections stained with Nissl: (F) 1 mm cleared brain slice, prefrontal cortex (PFC) area (left: $z = 1$ mm imaging stack depth); (G) 100 μ m uncleared brain slice, PFC (left: $z = 100$ μ m imaging stack depth); (H) 1 mm spinal cord slice ($z = 500$ μ m).

(I) Substantia nigra pars compacta (SNc) of 1 mm mouse brain slice stained with anti-tyrosine hydroxylase (TH) antibody ($z = 1$ mm).

(J) PFC of 1 mm adult mouse brain slices stained with antibodies against GFAP, mouse-IgG, and Iba1 ($z = 500$ μ m).

(K) 1 mm section of mouse kidney ($z = 150$ μ m; arrowheads show glomeruli), heart ($z = 320$ μ m), lung ($z = 550$ μ m), and 400 μ m section of mouse intestine ($z = 350$ μ m) stained with anti-integrin antibodies, SYTO24, and acridine orange.

(L) 3-mm-thick PACT-cleared human tissue biopsy from basal cell carcinoma (BCC) was stained with anti-pan-cytokeratin (AE1/AE3) Alexa Fluor 488 primary antibody and counterstained with DAPI to label endothelial cells (700 μ m imaging stack depth).

All graphs are shown in mean \pm SEM. Statistical significance: for paired samples: 2-tailed Student's *t* test; for multiple comparisons: one-way ANOVA followed by Bonferroni post hoc ($*p < 0.05$, $**p < 0.01$, $***p < 0.005$, and $****p < 0.0001$). Objectives used for confocal imaging: (F, left) Fluor 5 \times /0.25 M27 objective; (F, right, G, H, J, and K) LD LCI Plan-Apochromat 25 \times /0.8 Imm Corr DIC M27 multi-immersion objective; (I) LD SC Plan-Apochromat 20 \times /1.0 Corr M32 85 mm scale-immersion objective; (L) Zeiss Plan-Apochromat 10 \times /0.45 objective. Also see Figure S1, S2, and S3 and Tables S1 and S2.

integrity, and changes in weight and volume during clearing to ensure that a minimal crosslinking scheme was sufficient to preserve tissue morphology and molecular information. The amount of protein that leached out of tissue into SDS clearing buffer was statistically indistinguishable between 4% PFA-fixed, uncleared tissue samples (A0P4) that were incubated in PBS as a control, and cleared tissue-hydrogel matrices prepared with either 4% acrylamide (A4P0) or with 4% acrylamide plus 4% PFA (A4P4) (Figure 1C). Notably, the amount of protein recorded in the 8% SDS clearing bath solutions for all hydrogel-embedded samples was less than the protein loss (0.57 ± 0.11 mg per mg gross weight) for the samples preserved only with 4% PFA and incubated in PBS-0.1% Triton X-100, a mild detergent-containing buffer. This implies that hydrogel monomers effectively crosslink and stabilize tissue protein, which is further supported by our finding that unpolymerized, PFA-fixed tissue incubated in 8% SDS showed poor protein retention (0.63 ± 0.02 mg protein loss per mg gross weight) (Figure 1C).

To corroborate these results on the preservation of molecular content in PACT tissue, the relative levels of native eYFP fluorescence were visualized and quantified in PACT brain samples from Thy1-eYFP transgenic mice. While a decrease in mean fluorescence intensity was observed under both hydrogel formulations (A4P0, A2P0), PACT samples showed comparable total intensity relative to uncleared tissue (Figure 1D) once the fluorescent measurements were normalized for tissue expansion (Figure S1C). Indeed, tissue-hydrogel matrices that were prepared using acrylamide alone (A4P0) exhibited tissue weight and volume changes of $\sim 174\%$ and $\sim 223\%$, respectively (Figure 1E), which were significantly greater than the size changes of A4P4 counterparts. But, upon the transfer of tissue samples from clearing solution to mounting media, PACT samples shrank back to their original size within a few hours (Figure S3D). This tissue expansion-contraction has been documented in previous brain-clearing protocols (Chung et al., 2013; Hama et al., 2011; Susaki et al., 2014), wherein it was concluded that these size changes, though suboptimal, did not appear to negatively influence gross tissue morphology or cellular architecture. To visualize the effect of PFA on crosslink density in the tissue-hydrogel matrix, which is hypothesized to limit tissue expansion, PACT-cleared brain slices were imaged via scanning electron microscopy (SEM) (Figure S1B). We noted that A2P0 matrices had the largest pore sizes, followed by A4P0, while A4P4 had the smallest visualized pore sizes; pore size directly affects diffusion rate with faster macromolecular diffusion times in tissue-hydrogel matrices with larger pores. Tissue deformity (i.e., expansion and contraction) during PACT processing and mounting did not appear to affect the overall cellular organization or protein content of samples relative to conventional histological processing (Figures 1F–1L). Thus, we selected A4P0 for PACT given its balance between clearing speed, protein retention, and intermediate pore size, which is conducive to macromolecule tissue penetration during histology.

PACT Reagents Are Compatible with Histology and Endogenous Fluorochromes

To ensure that the signal intensity from genetically encoded fluorescent proteins was preserved throughout PACT processing,

1-mm-thick Thy1-eYFP tissue sections were A4P0-hybridized, PACT-cleared, and imaged using confocal microscopy. Despite PACT clearing, and importantly, the slow image acquisition time for thick samples, the genetically expressed eYFP was readily detected throughout the samples (Figures 1F and 1H). Furthermore, the tissue-hydrogel matrix still permitted uniform Nissl staining of thick, cleared sections (Figure 1F, compared to uncleared 100 μm sections in Figure 1G). The overall tissue architecture remained constant between cleared and uncleared sections, as revealed by Nissl staining (red), which assuages concern that successive swelling and then shrinking of tissue caused permanent tissue deformity.

Not only were native proteins, including those maintaining the structural integrity of tissue samples, retained by the tissue-hydrogel matrix during clearing (Figures 1C, 1F, and 1H), but also the cleared tissue blocks were sufficiently macromolecule permeable to permit labeling of peptidic and nucleic acid epitopes using a variety of common histological markers (e.g., antibodies, small-molecules, mRNA probes). For example, aside from Nissl, 1 mm PACT sections from the mouse brain and spinal cord were immunolabeled with antibodies against tyrosine hydroxylase (TH) (Figure 1I); glial fibrillary acidic protein (GFAP), murine immunoglobulin G (IgG), and ionized calcium-binding adaptor molecule 1 (Iba1) (Figure 1J). These targeted moieties represent antigens occupying a wide variety of cellular locations: membrane-localized and cytosolic, neuronal and non-neuronal antigens. PACT clearing decreased light scattering in tissue samples such that all labels were easily resolved across the entire 1 mm section during single-photon fluorescence imaging.

To confirm that PACT methodologies were effective on major organs as well, the kidney, heart, lung, and intestine of mice were excised, cleared, and labeled with anti-integrin antibodies, acridine orange (AO), and/or SYTO24 (Figure 1K). As observed in the central organ samples (Figures 1F and 1H–1J), small-molecule dyes and antibodies alike rapidly diffused through 1- to 3-mm-thick A4P0-crosslinked and PACT-cleared sections of organ tissues. While the time for complete immunolabeling of thick sections depends on several factors, including the tissue type, hydrogel pore size (Figure S1B), and the extent of lipid removal (Figures 1A, S1A), we achieved uniform 1° and 2° antibody penetration throughout PACT samples with a 7–12 day incubation. However, for studies that only require labeling with small-molecule fluorescent dyes, one may obtain rapid staining of 1–3 mm PACT brain sections with a single overnight to 3 day incubation, respectively. Some tissues were stained even faster: AO labeling of individual nuclei in unsectioned mouse intestinal tissue (~ 400 μm thick) was attained in under 1 hr (Figure 1K). We then determined if PACT can be applied to pathological samples. Human skin cancer biopsies (Figure S2A) were cleared and stained with pan-cytokeratin to visualize tumor cells (Figures 1L, S2B, and S2C). In sum, the entire PACT-cleared tissue block was accessible down to the subcellular level for molecular interrogation using standard immunohistochemical methods and conventional fluorescence microscopy.

To determine if PACT was compatible with established procedures to visualize single mRNA transcripts, we subjected PACT-processed tissue to single-molecule fluorescent in situ

hybridization, smFISH (Femino et al., 1998; Raj et al., 2008). The methodology of smFISH is capable of detecting single RNA molecules with high specificity in fixed cells, and its high sensitivity allows for measurements of RNA abundance and subcellular localization. However, smFISH in tissue sections remains challenging due to low signal to noise ratio caused by tissue autofluorescence. Herein, β -actin transcripts in 100- μ m-thick cleared mouse brain sections were labeled using 24 Alexa 594-labeled 20-mer oligonucleotide probes toward β -actin mRNA. Tissue samples were slide-mounted in media containing 4',6-diamidino-2-phenylindole (DAPI) and imaged via single-photon microscopy. β -actin transcripts were indeed retained in the cytoplasm of neurons throughout PACT and smFISH processing, and single points of fluorescence could be distinguished despite the high copy number of β -actin in cells and the considerable thickness of imaged brain section (Buxbaum et al., 2014; Raj et al., 2008) (Figure 2A). PACT tissue exhibited significantly increased contrast of diffraction-limited spots throughout the tissue relative to uncleared tissue (Figure 2C). We found that smFISH intensity showed very little difference between PACT cleared and uncleared tissue, while background intensity was significantly reduced (Figures 2A, 2B, 2D and 2E, and S2D). These findings, taken together with the increase in smFISH signal to noise ratio seen in PACT-cleared tissues, suggests that background autofluorescence in thick samples is the main factor obscuring smFISH signal in uncleared tissue.

Recipe for Refractive Index Matching Solution for Imaging and Long-Term Storage of Cleared Tissue

Effective imaging relies on sample immersion in a mounting media that reduces the refractive index (RI) variations within heterogeneous tissue and that alleviates the RI mismatch between tissue, mounting media, and lens immersion media interfaces. In response to the prohibitive cost and limited availability of FocusClear, we formulated an affordable substitute: RIMS, with an RI appropriate for tissue imaging (RI = 1.38–1.48), biological safety, and biocompatibility for tissue preservation (see Extended Experimental Procedures). To test RIMS, PACT-processed samples were mounted in 80% glycerol, FocusClear, or RIMS, and then imaged under identical conditions (Figure S3A). RIMS provided good optical clarity for fluorescence microscopy (Figure S3C) and caused minimal quenching of the eYFP signal over a 3 month period (Figure S3E). Since its performance appeared to be on par with or exceed FocusClear (Figure S3A) and provided a >10-fold reduction in mounting costs, RIMS was employed for all subsequent PACT and PARS experiments. The exact RIMS formulation can be optimized in a case-specific manner depending on the tissue samples and microscopy set-up (Figure S3B).

Whole-Body Clearing Using the Vasculature in Adult Rodents

The PACT protocol uses a 4% acrylamide monomer solution to generate the final tissue hydrogel and results in a good combination of protein preservation, speed and ease of clearing, and optical clarity. However passive diffusion is slow, prohibitive for large volume or whole-organism clearing. We also noted that the acrylamide hydrogels markedly swelled during the detergent-clearing phase (Figures 1A and S1C). These two draw-

backs, common to most clearing protocols, prompted us to develop an alternate methodology to speed up clearing and also to minimize tissue expansion during clearing. We decided to utilize the existing vasculature networks, as is done regularly in cardiac perfusion fixation (Gage et al., 2012; Jonkers et al., 1984), to introduce agents directly to tissue by performing the entire fixation and clearing procedure in situ. We term this method perfusion-assisted agent release in situ (or PARS). PARS utilizes the intact vasculature of the animal to infuse the hydrogel monomer and clearing solutions directly, which then diffuse throughout the tissues of interest.

To investigate both whether major blood vessels and whole-organism microvasculature was accessed by the perfusate (Leong and Ling, 1990; Li et al., 2012), AlexaFluor 647-conjugated antibodies against mouse immunoglobulin (Figure S4B, right) or Atto 488-conjugated nanobodies against GFAP (Figure S4B, left) were perfusion recirculated through cardiac catheters for 24 hr. The mouse brain vasculature was extensively labeled, illustrating the accessibility of blood vessels to perfusate (Figure S4B). Perfusate was also observed to diffuse into surrounding tissue, as shown by the extravasculature GFAP labeling (Figure S4B, Movie S1).

To perfuse PACT reagents in the cerebrospinal or systemic circulation for several days-to-weeks, we developed a closed-loop perfusion system. Using this custom PARS chamber (Figure S4A), continuous intracranial perfusion of 8% SDS into cerebrospinal fluid (CSF), via a method we termed PARS-CSF (Figure 3), attained modest whole-brain clearing in as little as 4 days (Figures 3A and 3B). Inserting the cannula more caudally above the inferior colliculus (Figure 3A, right) granted clearing of the entire length of the rat spinal cord in 2 weeks (Figure 3B). Next, AAV9-eGFP injected adult mice were prepared with a subdural cannula inserted directly above the olfactory bulb (Figure 3A, left), and after 4 days of recirculating 8% SDS at 37 °C, both unmyelinated and densely myelinated mouse brain regions near CSF circulation (most parts of the cortex, hypothalamus, regions near the ventricles and spinal cord) were transparentized. GFP-labeling of individual neurons, neuronal processes, and glial cells was clearly visible throughout the brain (Figure 3C).

Herein, we surmised that the same perfusion-clearing method of PARS-CSF could be extended to clearing whole-bodies in situ. Furthermore, the application of a pressure gradient on tissue during the lipid extraction and antibody diffusion, respectively, might hold the added benefit of accelerating the clearing and immunolabeling steps relative to PACT-based clearing of individual excised whole-organs. Clearing reagents were cycled through systemic circulation (see timeline, Figure 4A), with complete clearing of all major organs and of central nervous system accomplished within 1 week and 2 weeks, respectively, for mice and rats alike (Figures 4B–4D and S7). The minimal protein content of the PARS perfusate, and the higher protein content of perfusate from AOP4-infused mice (Figure 4E) suggested that the whole-organism hydrogel matrix was both necessary and sufficient to stabilize gross organ structure and macromolecular content. To confirm that PARS was compatible with visualizing localized fluorescent protein expression in sparsely labeled cells in multiple organs, we delivered a GFP transgene by systemic administration of

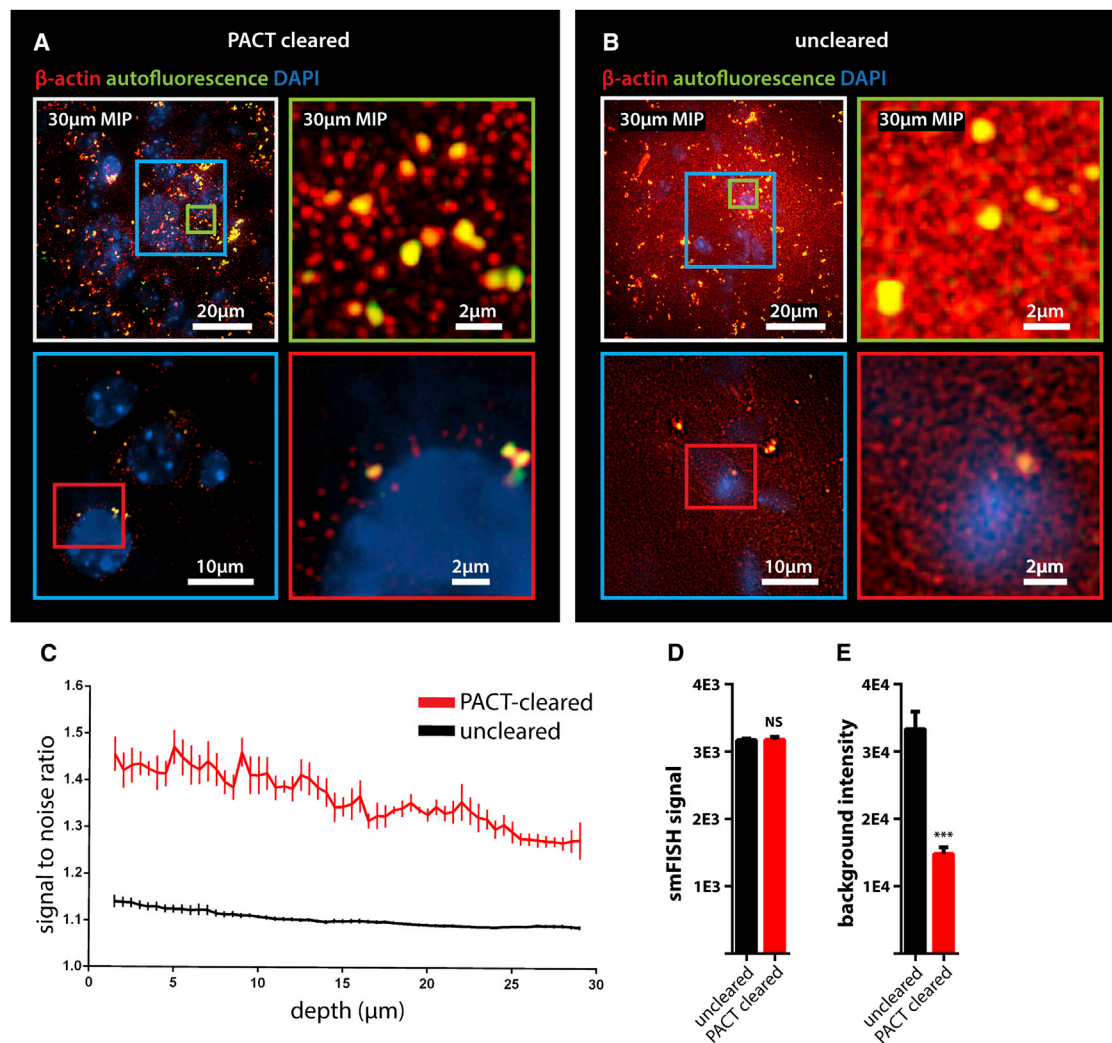


Figure 2. Detection of Individual mRNA Transcripts in PACT Tissue Sections by smFISH

(A and B) 100- μm -thick mouse brain slices were hybridized with twenty-four 20-mer oligonucleotide probes toward β -actin mRNA labeled with Alexafluor 594. (A) PACT-cleared smFISH brain slices. Top shows 30 μm maximum intensity projection. An abundant number of diffraction limited spots corresponding to single β -actin mRNAs (red) were readily detected up to 30 μm in depth under 589 nm illumination. Note bright amorphous granules (yellow) are background lipofuscin vesicles that show up in both 589 nm (red) and 532 nm autofluorescence (green) channels, whereas smFISH signals are in the red channel only. (B) Compared to PACT-cleared slices, smFISH in uncleared brain slices showed significantly decreased contrast. (Bottom in A and B show single slices of 0.5 μm at 12 μm depth; the images were processed from raw data using the same contrast scale and Laplacian of Gaussian filtering; for raw data see Figure S2D).

(C) Signal to noise ratio as a function of depth shows PACT-clearing tissue increases the signal to noise ratio of smFISH throughout the thickness of the sample as compared to uncleared tissue.

(D) smFISH intensities show no appreciable differences between uncleared and PACT-cleared tissue. $p = 0.8722$; 2-tailed Student's t test.

(E) Comparison of background intensity between uncleared and PACT-cleared tissue illustrates the significant reduction of background fluorescence in PACT-cleared tissue.

$p = 0.0006$; 2-tailed Student's t test. All graphs are shown in mean \pm SEM. Imaging set-up: (A and B) samples imaged on a Nikon Ti Eclipse microscope with an Andor Ikon-M camera and a 60 \times /1.4NA Plan Apo λ objective with an additional 1.5 \times magnification. Images acquired as Z-stacks with a 0.5 μm step size over 30 μm . Samples were excited by a 640 nm Coherent Cube, and 532 nm (SDL-532-200TG) and 405 nm (SDL-405-LM-030) lasers.

adeno-associated virus (AAV). AAV9:CAG-eGFP (Figure 5D) or AAV9BD1:CAG-eGFP, a variant of AAV9 that transduces CNS neurons to a similar extent as AAV9, but exhibits reduced astrocyte and hepatocyte transduction (Figure 5E) was delivered via the vasculature in adult mice. In both the brain and the liver, native eGFP expression was readily detectable and the reduced transduction of liver hepatocytes by AAV9BD1

as compared with AAV9 was easily detected (Figures 5E versus 5D).

In comparison to PACT, we predicted that tissue volume changes during PARS processing would be reduced since musculoskeletal structures, such as the skull, the vertebral column, and muscle walls, would physically constrain tissue expansion. Indeed, PARS-based clearing of rodent brains was

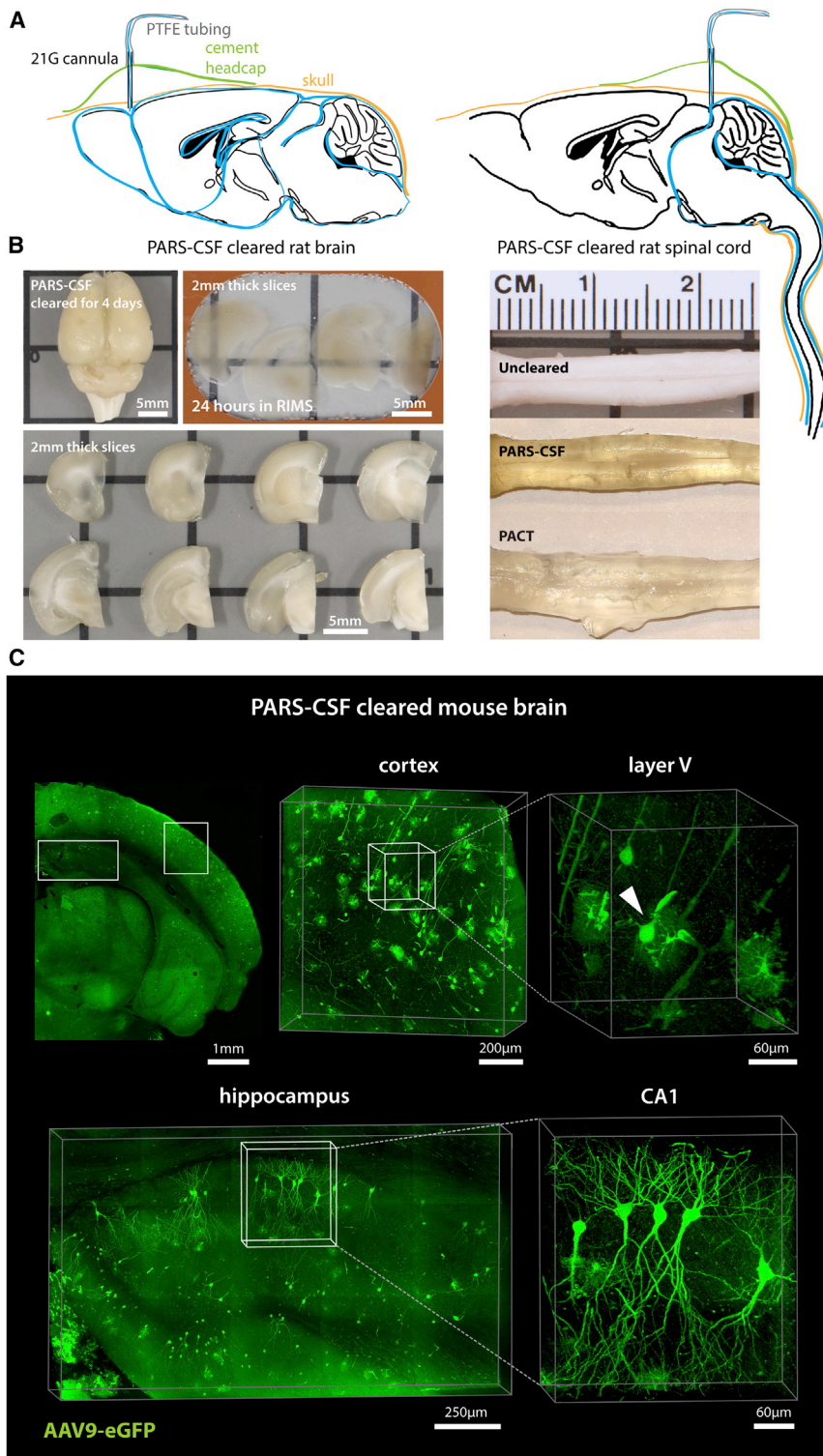


Figure 3. PARS-CSF: A Protocol for Rapid Brain or Spinal Cord Clearing and Labeling via the Cerebrospinal Fluid Circulation Using Perfusion-Assisted Agent Release In Situ

(A) CNS tissue may be rendered optically transparent by the direct perfusion of all PACT reagents into the CSF via an intracranial brain shunt inserted either (left) below the dura in the region directly above the olfactory bulb, or (right) placed directly above the dorsal inferior colliculus. The cannula, which is connected to the perfusion lines may be cemented into position with dental acrylic.

(B) Whole-brain and the corresponding 2-mm-thick slices (left) and whole-spinal cord (right) from PARS-CSF rats that were cleared at 37°C for 4 days (brain) or for 2 weeks (spinal cord) are shown. The extent of whole-brain clearing is dependent on brain tissue proximity to the cannula: the frontal lobe was rendered optically transparent, whereas the midhind brain were only weakly cleared (see 2 mm slices on right side of panel). After 24 hr incubation in RIMS, PARS-CSF brain slices were sufficiently cleared for imaging without further sectioning.

(C) Images show native eGFP fluorescence in 500 μm PARS-CSF-cleared coronal brain slices prepared from mice that, 6 months prior to clearing, received IV injections with AAV9:CAG-eGFP. Representative sections of cortex and hippocampus are presented at higher magnification in image boxes (right). In the layer V coronal view, an AAV9 transduced eGFP-expressing glial cell and eGFP-neuron adjacent to a blood vessel are clearly visible. In the hippocampus (bottom), the finer neuronal processes of eGFP-expressing CA1 neurons may be visualized with high resolution, which suggests that PARS-CSF may be completed without severe damage to cellular morphology.

Objectives used for confocal imaging: (C) LD LCI Plan-Apochromat 25x/0.8 Imm Corr DIC M27 multi-immersion objective. Also see [Figure S4](#).

there was no evidence to suggest that gross changes in neuronal morphology occurred as a result of PARS processing and post-PARS expansion ([Figure 5B](#)). Nevertheless, we attempted to mitigate tissue swelling in RIMS through postfixing PARS samples in 4% PFA overnight prior to RIMS mounting. To assess the extent to which overall tissue architecture was altered by volume changes, the intercellular distance and the average cell size within different brain regions (cortex, striatum, thalamus) of uncleared, PARS-

cleared, and postfixed PARS-cleared samples were measured ([Figure S5B](#)). It was predicted that individual regions may be differentially affected by PARS processing or RIMS incubation; for example, any sheer forces originating from perfusion-related

accomplished with limited hydrogel swelling and tissue expansion during clearing ([Figures 4C and 4D and S5A](#)). Although PARS-processed brains do swell slightly following their extraction from the skull and placement in PBS or RIMS ([Figure S5A](#),

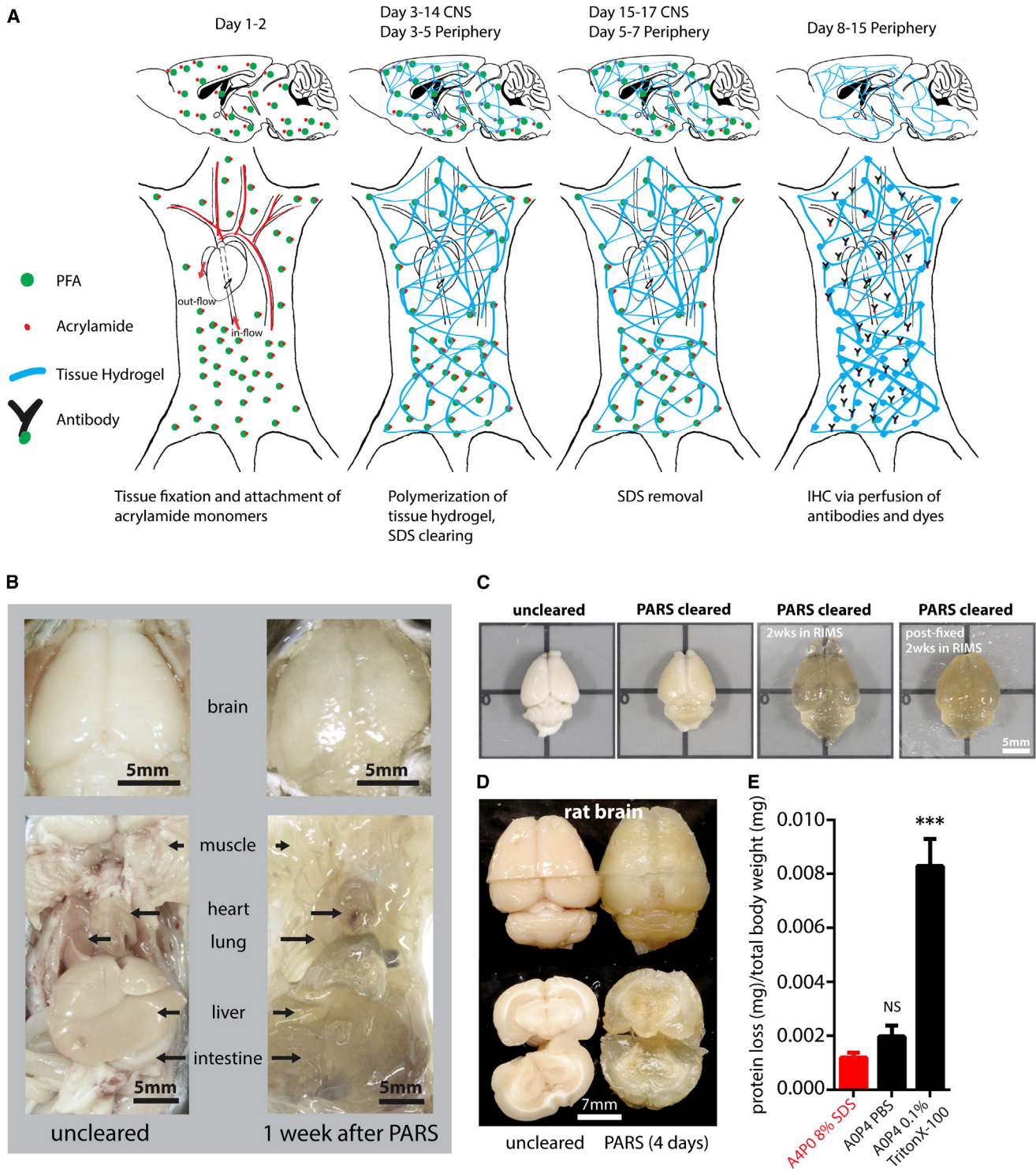


Figure 4. PARS Achieves Whole-Body Clearing

(A) Schematic of PARS clearing and immunostaining.

(B) A comparison of optical transparency of mouse brains and major organs before and after PARS clearing.

(C) Representative images of relative mouse brain size before (first box, from left) and after (second box) 2 weeks of PARS clearing shows that PARS circumvents hydrogel swelling and brain tissue expansion during the clearing process. Brain tissue expands gradually after immersion in RIMS (third box); this volume change may be mitigated via postfixing PARS samples in 4% PFA overnight prior to RIMS mounting (fourth box).

(legend continued on next page)

intracranial pressure may exert a greater insult on less myelinated tissue or cause ventricle collapse. Postfixing PARS samples significantly prevented the increased cell sizes and intercellular distances that were detected throughout PARS samples. There were no significant differences in cell size or intercellular spacing between uncleared and postfixated samples in all brain regions assayed (Figure S5B).

Whole-Organism PARS Enables Phenotyping and Imaging in an Organ-by-Organ Fashion

Following whole-body PARS processing and labeling, major organs were excised, thick-sectioned, and imaged using confocal microscopy (Figures 5, 6, and S6). The PARS-cleared whole brain (Figures 5A and 5B) and spinal cord (Figure 5C) of Thy1-eYFP mice were imaged, and we concluded that PARS processing rendered entire organs optically transparent to the extent that visualizing deep-tissue structures with cellular resolution was possible. Through visualizing individual neurons and nephrons throughout the cleared whole-brain (Figures 5A and 5B; Movie S2) and kidney (Figure 6B; Movie S3), respectively, we may posit that this optical clarity was achieved while leaving fine cellular structures intact, in part due to the success of in situ tissue-hydrogel polymerization in stabilizing tissue architecture, preserving protein content and endogenous fluorescence, and maintaining the spatial relationships between subcellular and cellular tissue components (Figures 5A and 5B). For example, we could resolve individual fluorescently labeled glomeruli of individual nephrons within whole-kidney, which establishes the ability of PARS to access major organs through intact vasculature (Figures 6B and S6). Importantly, this includes the delivery of all immunohistochemical solutions as well, including blocking solutions, primary and fluorescently labeled secondary antibody cocktails, or fluorescently labeled small-molecules, and wash buffers. Labeling using PARS was target-specific, uniformly distributed throughout major organs, and exhibited low background; this was illustrated by the anti-tubulin antibody and DRAQ5 labeling in PARS-processed mouse kidney (Figure 6B, Movie S2) and by the lectin staining of blood vessel endothelium in the liver, lung, and pancreas (Figure S6).

DISCUSSION

Herein we introduce PARS, a method that renders intact whole-organisms transparent for imaging with single-cell resolution while preserving fluorescent and protein-based signals and tissue architecture. Our starting point, the CLARITY method (Chung et al., 2013) provided scientists with a brain-processing platform for elucidating the 3D cellular arrangement and connectome in toto. Numerous laboratories have previously reported on new clearing reagents in the decade before CLARITY; however, many of these reagents were highly appli-

cation or tissue specific (summarized in Table S1). In contrast, CLARITY introduced two broadly applicable techniques pertaining to tissue preservation (hydrogel embedding) and clearing efficiency (electrophoretic tissue clearing, ETC), both of which could be incorporated into the design, or redesign, of other clearing procedures. Traditionally, making tissue transparent was a process that demanded solvent incubations on the order of weeks to months, as reported in other clearing protocols (Hama et al., 2011). ETC, however, challenged the prevailing view that the rate of tissue clearing could only be accelerated through assaying large panels of organic solvents for their ability to solubilize tissue rapidly. Oftentimes, candidate solvents tested in these screens achieved rapid tissue clearing, but compromised tissue structure (Hama et al., 2011) or quenched native fluorescence (Becker et al., 2012; Ertürk et al., 2012a; Susaki et al., 2014). Although the reagents introduced by CLARITY are gentler by comparison, the needed ETC step for fast clearing can cause tissue degradation from sample heating. This risk can be bypassed by the use of passive CLARITY (Tomer et al., 2014), but again, the slow rate of clearing makes the technique impractical for scaling up or for whole-body mapping.

With the goal of rapidly clearing whole organisms while still using mild detergents and fluorescence nonquenching reagents throughout, we evolved PARS on the basic principles of CLARITY, but aimed to bypass the need for ETC while maintaining faster clearing than through passive diffusion. First we optimized the CLARITY agents for passive clearing by removing bisacrylamide and increasing the detergent concentration to 8% SDS (PACT reagents). The tissue-clearing step was redesigned such that the electrophoretic force used by CLARITY to drive fast lipid extraction was replaced with a perfusion-based pressure gradient. Controlled flow of PACT reagents throughout intact tissue vasculature transforms most organs into optically transparent tissue within 2–3 days, while whole-mouse and whole-rat brains are rendered transparent within 1–2 weeks. Additionally, the self-contained nature of clearing in situ also reduced tissue expansion during monomer infusion and lipid removal.

PARS opens up the possibility of whole-organ and whole-organism mapping with high phenotypic content. With this in mind, quick, low-resolution scanning of large tissue blocks can direct investigators to restricted areas worthy of slow, high phenotypic content analysis, including smFISH: a method that preserves fluorescent markers long-term is particularly valuable in this respect. Both PACT and PARS methodologies are scalable, cost-effective relative to the original CLARITY process and theoretically transferable to other model organisms or human tissue. Indeed, while PARS was depicted using cardiac perfusion in rodents, the overall methodology may also be applicable to instances in which sufficiently large vessels are available for creating a perfusion route, such as whole-organ perfusion in

(D) Representative images of relative rat brain size before (right) and after (left) 4 days of PARS clearing, showing how PARS is a scalable method. Coronal slices of rat whole-brain samples show gross tissue morphology, highlighting that unmyelinated areas may be cleared within 4 days of PARS-based clearing.

(E) Protein loss of PARS clearing compared to other clearing methods ($n = 4$ mice for each); graph shows mean \pm SEM; one way ANOVA followed by Bonferroni post hoc test was used to determine statistical significance in comparison to A4P0 8% SDS PARS clearing; *** $p < 0.005$.

Images for (B–D) were taken using bright field camera. Also see Figures S4, S7, S3E, and Movie S1.

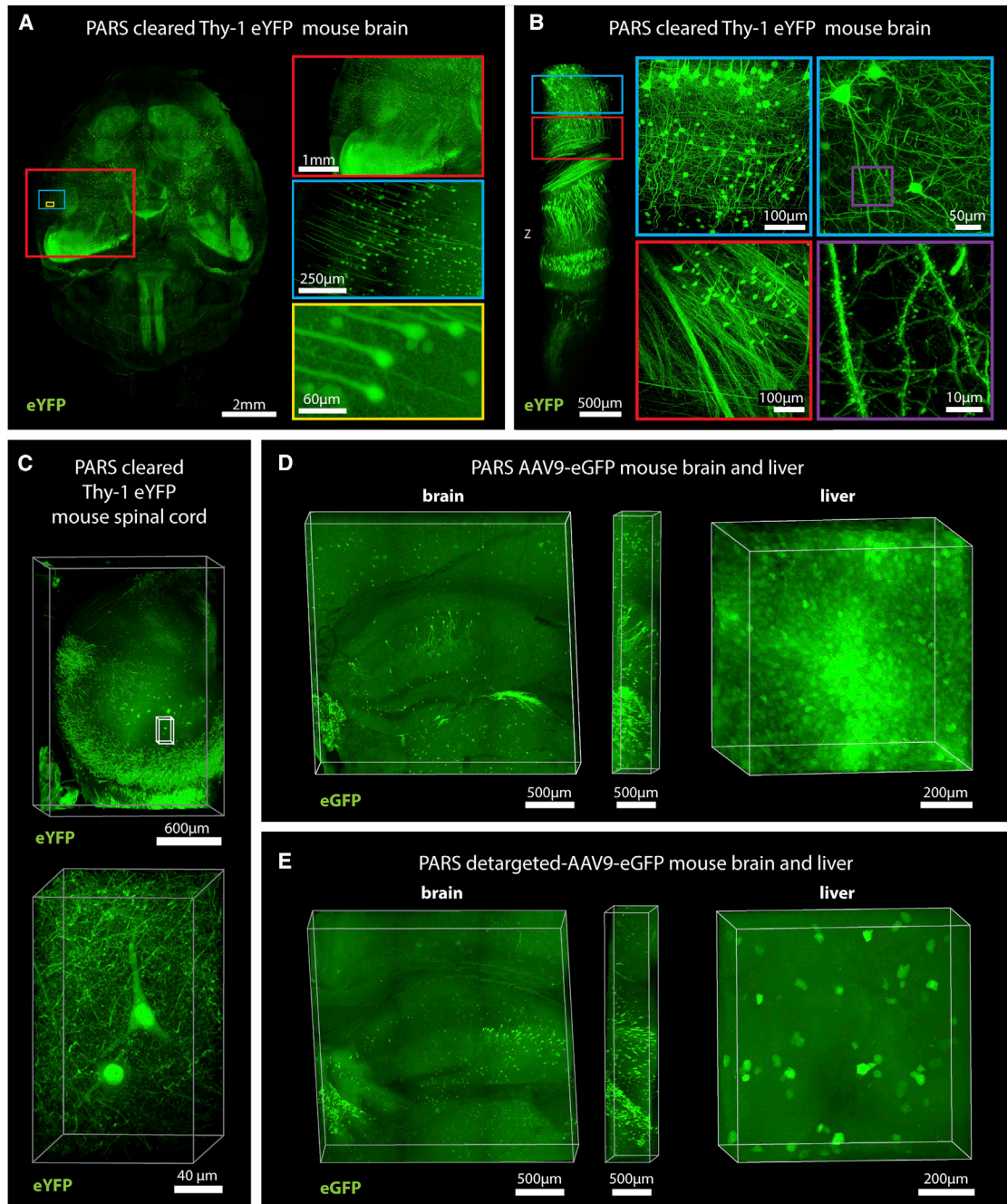


Figure 5. PARS Enables Whole-Brain Mapping of Widespread and Sparse Genetically Encoded Fluorescent Signals with Subcellular Resolution

(A and B) Whole-brain image ($z = 6$ mm) (A), and deep-brain imaging ($z = 4$ mm) (B) of adult Thy1-eYFP mouse after PARS clearing for 10 days. The boxes on the right show high-magnification images of indicated areas.

(C) Spinal cord image of adult Thy1-eYFP mouse after PARS clearing for 2 weeks ($z = 2$ mm). Bottom, high-magnification images of indicated region ($z = 1.2$ mm).

(D) Images show native eGFP fluorescence in 1 mm coronal brain slices (left) and liver (right) prepared from the PARS-cleared mice that received IV injections of AAV9:CAG-eGFP. Image columns to the right of each coronal brain image show the orthogonal views ($z = 0.5$ mm).

(E) Native eGFP fluorescence in 1 mm coronal brain slices (left) and liver (right) prepared from PARS-cleared mice injected with a liver detargeted variant, AAV9BD1:CAG-eGFP. Image columns to the right of each coronal brain image show the orthogonal views ($z = 0.5$ mm).

Objectives used for confocal imaging: (A) Fluor 5 \times /0.25 M27 objective; (B) Leica HC FLUOTAR L 25 \times /1.00 IMM CORR objective working distance of 6.0 mm; (C, Top) Fluor 5 \times /0.25 M27 objective (C, Bottom, inset) LD LCI Plan-Apochromat 25 \times /0.8 Imm Corr DIC M27 multi-immersion objective; (D–E) LD LCI Plan-Apochromat 25 \times /0.8 Imm Corr DIC M27 multi-immersion objective. Also see [Figure S5](#) and [Movie S2](#) (for 5B).

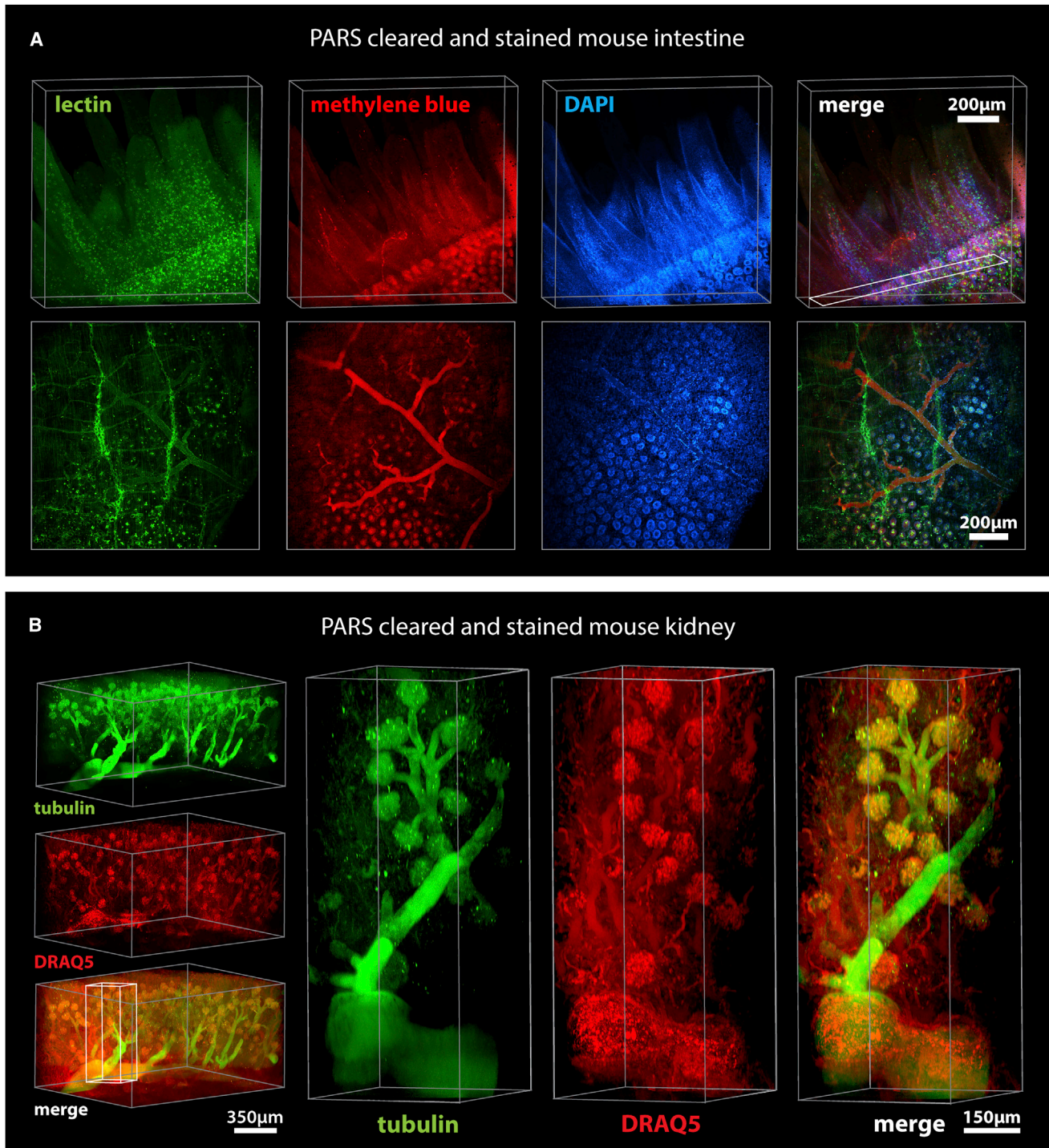


Figure 6. PARS Allows Rapid and Uniform Clearing and Immunolabeling of Major Organs

(A and B) Clearing and immunohistochemical labeling was achieved in whole mice through PARS alone. (A) PARS-cleared mouse intestine was stained with lectin, methylene blue, and DAPI, and imaged through a depth of 500 μ m. Bottom row, maximum intensity projection of slice outlined within top-right rendering, $z = 50 \mu$ m. ($z = 500 \mu$ m). (B) A whole kidney was imaged (left) for anti-tubulin antibody and DRAQ5 labeling. High-magnification images (right) of the indicated region and the structure of glomeruli, demonstrating that PARS enables antibody-based labeling throughout the kidney ($z = 1.2$ mm). Objectives used for confocal imaging: (A) Zeiss LSM 780 confocal microscope with the 10 \times 0.45 N.A. Plan-Apochromat; (B) LD SC Plan-Apochromat 20 \times /1.0 Corr M32 85 mm scale-immersion objective (working distance 5.6 mm, Zeiss). Also see [Figure S6](#), [S7](#), and [Movie S3](#) (for 6B).

larger, higher-order mammals, including isolated human tissue. While PARS does achieve increased speed of clearing and reduced swelling without tissue damage (Table S1) the method's unique strength lies in its scalability. Our data demonstrate, for example, that PARS can be employed to assess AAV-mediated transduction at the cellular level in multiple organs after systemic delivery. By eliminating the need to section individual tissues, the PARS approach could expedite efforts to screen numerous AAV serotypes and/or gene regulatory elements for optimal expression in the cell types of interest. In addition to improving screening throughput and speed, a PARS-based whole-body method could also counteract the risk of underestimating AAV transduction in target tissues due to undersampling errors.

PARS holds the potential to refine our understanding of peripheral nerves at their target whole organs. Accurate maps of complex long-range fiber bundles, such as for the vagus nerve (George et al., 2000), could help inform improvements in existing therapies or spur the development of entirely novel therapeutic strategies, such as for bioelectronic medicines (Famm et al., 2013). Expanding this strategy out to the level of body-brain interconnections, PARS may facilitate biomedical work in whole-body screening experiments for off- and on-target agents, and for sparse elements such as metastatic tumor cells or stem cells. Lastly, the PARS method is compatible with cell-filling endoskeletal structures. By combining PARS with TEMPEST—a precursor to CLARITY (Deisseroth and Gradinaru, 2012)—the in vivo expression of long-lasting keratin filaments (that outline the cells themselves while keeping a loyal blueprint of the morphology) within populations of interest can facilitate accurate postmortem quantification and mapping of long-degenerated cells throughout the brain.

The methods introduced here build upon our prior work using CLARITY to expand tissue clearing and phenotyping to whole organisms by using the intrinsic circulatory systems. Because the vascular network is not homogeneous, leading to nonuniform perfusive flow, organs of interest will clear at different rates. To achieve optimal clearing while retaining high tissue content, further validation for specific applications and technical improvements will be necessary. The blood-brain barrier may present a challenge to efficient perfusion-based transport of particularly large molecules such as antibodies (150 kDa) to the brain relative to the other organs. To improve perfusion efficiency, one likely solution will be to engineer (or utilize when already available) smaller antibody scaffolds for immunolabeling; these include the fragment-antigen-binding format of immunoglobulins (Fab ~50 kDa), and nanobodies, single domain antibodies derived from camelid antibodies, whose smaller size (~12–15 kDa) promotes tissue permeability (Harmsen and De Haard, 2007).

Improved imaging platforms will be needed to take full advantage of all the recent tissue-clearing work, ours and others (Becker et al., 2012; Chung et al., 2013; Dodt et al., 2007; Ertürk et al., 2012a; Ertürk and Bradke, 2013; Hama et al., 2011; Ke et al., 2013; Kuwajima et al., 2013; Susaki et al., 2014). In order to obtain cellular and subcellular information in thick cleared tissue, it is necessary to utilize long-working distance, high numerical aperture, multi-immersion objectives. Scanning speed is an additional barrier with cleared tissue blocks taking many days to be fully imaged—resonant scanners or light-sheet microscopy

(Tomer et al., 2014) can accelerate the process while retaining high-resolution data.

Given increasing interest in the link between the brain and major organ systems (Birmingham et al., 2014), it will be critical to have an unsegmented view of the whole body, with structural connections between the brain and other major organs left intact. The combination of PARS with enabling technologies (nanobodies, imaging platforms) will not only advance neuroscientists' overarching goal of creating a brain connectome, but it also has the potential to facilitate mapping the broader brain-to-body-and-back connectome and phenotyping other organ systems in the body, healthy or diseased.

EXPERIMENTAL PROCEDURES

PACT Clearing

Four percent paraformaldehyde (PFA)-fixed tissue sections were incubated at 4°C overnight in the hydrogel monomer solution A4P0 (4% acrylamide in PBS) supplemented with 0.25% photoinitiator 2,2'-Azobis[2-(2-imidazolin-2-yl)propane]dihydrochloride (VA-044, Wako Chemicals USA). A4P0-infused samples were degassed with nitrogen for 1–5 min and then incubated for 2–3 hr at 37°C to initiate tissue-hydrogel hybridization. After removing excess hydrogel via brief PBS washes, tissue-hydrogel matrices were transferred into 50 ml conical tubes containing 8% SDS in 0.1 M PBS (pH 7.5), and depending on tissue size, were incubated for 2–5 days at 37°C with shaking. For immunostaining, 1- to 3-mm-thick PACT-processed samples were washed in PBS with 4–5 buffer changes over the course of a day and then transferred to buffer containing small-molecule dyes or primary antibodies followed by fluorescently conjugated secondary antibody (1:200–400, in PBS containing 2% normal donkey serum, 0.1% Triton X-100 and 0.01% sodium azide) for 3–7 days or with small-molecule dyes for 1–3 days. Antibody or small-molecule dye solutions need to be replaced every day. Unbound antibody was removed via PBS washes, as before, and then samples were incubated with secondary antibodies (Fab fragment secondary antibodies are preferred, 1:200–400) for 2–5 days then washed for 1 day in PBS or phosphate buffer (PB) prior to incubation in imaging media (RIMS). All staining and mounting steps were conducted at room temperature with gentle shaking.

RIMS Imaging Media with RI 1.46

Forty grams of Sigma D2158 (Histodenz) in 30 ml of 0.02 M PB with 0.1% tween-20 and 0.01% sodium azide, pH to 7.5 with NaOH—which results in a final concentration of 88% Histodenz w/v. Samples are incubated in RIMS until transparent (~1 day for PACT samples, up to 1 week for PARS-cleared brains), followed by mounting in fresh RIMS.

smFISH

One hundred micrometer PACT sections were ethanol-permeabilized, labeled with 24 Alexa 594-labeled 20-mer oligo probes toward *β-actin* (overnight incubation at 37°C), washed, and coverslipped with Slowfade Gold + DAPI according to published protocols (Buxbaum et al., 2014; Lyubimova et al., 2013). Laplacian of Gaussian filtering with a radius of 3 was applied to visualize transcripts in both cleared and uncleared samples.

PARS Protocol

Immediately following standard cardiac perfusion with 4% PFA (in PBS, pH 7.5), the fixed rodent was transferred onto a perfusion chamber (Figure S4A) which recirculated all subsequent PACT and immunolabeling reagents (as above) continuously (1 ml/min) through rodent vasculature via a peristaltic pump. Perfusion tubing connected the chamber to a feeding needle inserted through the left ventricle into the aorta and loosely sutured in place. The rodent was postfixed with 4% PFA for 1 hr and then perfusion washed with PBS for 1 hr. A4P0 monomer was cycled through vasculature overnight, followed by a 2 hr PBS perfusion wash. Before polymerization and without disconnecting perfusion lines, the perfusion chamber was placed into a ziplock bag (Figure S4A), and the bag containing the chamber with rodent was degassed for

2 min under nitrogen gas. Polymerization was initiated via perfusion recirculation of 200 ml of 0.25% VA-044 initiator in PBS at 37°C for 2–3 hr. The whole-body was cleared through a ≤ 2 week perfusion with 8% SDS in PBS, pH 7.5 at 37°C–42°C followed by extensive PBS perfusion washing over 2–3 days. Antibodies and small-molecule dyes (as above in PACT) were then delivered via a 3 day perfusion and 1 day wash.

For the PARS-CSF variation of brain or spinal cord clearing (Figures 3A and 3B), transcardially-fixed rodents were decapitated and a subdural cannula was inserted above the region of interest and cemented to the skull. All PACT reagents are delivered in the same order and timeframe as PARS at 1 ml/min.

AAV Production and Systemic Delivery

Single-stranded ssAAV-CAG-eGFP vectors packaged into AAV9 or the AAV9 variant capsid, AAV2/9BD1, was generated and purified as described (Lock et al., 2010). The AAV2/9BD1 capsid was modified from AAV2/9 (U. Penn) with, among others, an N498Y mutation to reduce liver transduction (Pulicherla et al., 2011); 1×10^{12} vector genomes (vg) of either virus was delivered intravenously into mice and tissue assessed 6 months later by PARS for native eGFP fluorescence.

Fluorescence Microscopy

Cleared tissue samples were mounted in RIMS at room temperature using spacers from 0.5–7 mm depending on sample thickness (iSpacer, SunJin Lab; Silicone Isolator, Electron Microscopy Sciences, PA) and coverslipped. For Figure 3B, the samples were imaged by Leica Microsystems using a Leica TCS SP8 two-photon microscope with the Leica HC FLUOTAR L 25 \times /1.00 IMM CORR objective (working distance, w.d. 6.0 mm). Other images were taken using a Zeiss LSM 780 confocal microscope with either the Fluar 5 \times /0.25 M27 objective (w.d. 12.5 mm), Plan-Apochromat 10 \times /0.45 M27 objective (w.d. 2.0 mm), LD SC Plan-Apochromat 20 \times /1.0 Corr M32 85 mm scale-immersion objective (w.d. 5.6 mm), or LD LCI Plan-Apochromat 25 \times /0.8 Imm Corr DIC M27 multi-immersion objective (w.d. 0.57 mm). Image reconstructions were performed using Imaris imaging software (Bitplane). After imaging, samples were stored in RIMS at room temperature.

For more detailed methods see [Extended Experimental Procedures](#) and [Table S2](#) for a detailed list of reagents/buffers.

SUPPLEMENTAL INFORMATION

Supplemental Information includes Extended Experimental Procedures, seven figures, two tables, and three movies and can be found with this article online at <http://dx.doi.org/10.1016/j.cell.2014.07.017>.

AUTHOR CONTRIBUTION

B.Y., J.B.T., and V.G. conceived the project. B.Y., J.B.T., R.P.K., B.E.D., C.-K.C., E.L., S.S., L.C., and V.G. planned and executed experiments. B.Y., J.B.T., V.G. made the figures and wrote the paper with input from all other authors. V.G. supervised all aspects of the work.

ACKNOWLEDGMENTS

We thank the entire Gradinaru lab for helpful discussions. We also thank Drs. Dianne Newman and David Anderson for helpful discussions and suggestions. We thank Drs. Amir Arbabi and Andrei Faraon for assistance with SEM imaging. We thank Richard Bennett and Erik Cabral for assistance with tumor procurement. We thank Leica Microsystems for acquiring some of the images presented with a Leica TCS SP8 with Leica HC FLUOTAR L 25 \times /1.00 IMM CORR objective designed for CLARITY imaging. B.D. and V.G. especially wish to acknowledge the contributions of Paul H. Patterson (1943–2014), whose desire to apply tissue clearing to unresolved questions in neuroscience pushed us to further evolve these methods. This work was funded by: the NIH/NINDS New Innovator (NIH IDP20D017782-01); NIH 1R01AG047664-01; Startup funds from the President and Provost of California Institute of Technology and the Biology and Biological Engineering Division of California Institute

of Technology; the Beckman Institute of Caltech; the Pew Charitable Trust; the Sidney Kimmel Foundation (to V.G.). And NIH R01HD075605 (to L.C.). V.G. is also supported by: Human Frontiers in Science Program, the Mallinckrodt Foundation, the Gordon and Betty Moore Foundation, the Michael J. Fox Foundation, Caltech-GIST, NIH 1R01NS085910-01, NIH 1R21MH103824-01. C.-K.C., S.S., E.L., acknowledge support from the Caltech Biology Division Training grant (NIH/NRSA 5T32GM07616). R.P.K. acknowledges support from NIH/NIAMS (5T32AR058921). J.B.T. acknowledges the Colvin Postdoctoral Fellowship and CALTECH Division of BBE. B.Y. and V.G. have disclosed these methods and findings to the Caltech Office of Technology Transfer (CIT File No.: CIT-6686-P). V.G. is a cofounder of Circuit Therapeutics and holds related IP and stock (less than 5%). At this writing, V.G. receives no research funding, royalties, or consultant fees from any for-profit organization.

Received: May 6, 2014

Revised: July 13, 2014

Accepted: July 15, 2014

Published: July 31, 2014

REFERENCES

- Becker, K., Jährling, N., Saghafi, S., Weiler, R., and Dodt, H.U. (2012). Chemical clearing and dehydration of GFP expressing mouse brains. *PLoS ONE* 7, e33916.
- Becker, K., Jährling, N., Saghafi, S., and Dodt, H.U. (2013). Ultramicroscopy: light-sheet-based microscopy for imaging centimeter-sized objects with micrometer resolution. *Cold Spring Harbor protocols* 2013, 704–713.
- Buxbaum, A.R., Wu, B., and Singer, R.H. (2014). Single β -actin mRNA detection in neurons reveals a mechanism for regulating its translatability. *Science* 343, 419–422.
- Chung, K., and Deisseroth, K. (2013). CLARITY for mapping the nervous system. *Nat. Methods* 10, 508–513.
- Chung, K., Wallace, J., Kim, S.Y., Kalyanasundaram, S., Andalman, A.S., Davidson, T.J., Mirzabekov, J.J., Zalocusky, K.A., Mattis, J., Denisin, A.K., et al. (2013). Structural and molecular interrogation of intact biological systems. *Nature* 497, 332–337.
- Deisseroth, K.A., and Gradinaru, V. (2012). Functional Targeted Brain Endoskeletonization. U.S. patent US2014030192.
- Dodt, H.-U., Leischner, U., Schierloh, A., Jährling, N., Mauch, C.P., Deininger, K., Deussing, J.M., Eder, M., Zieglgänsberger, W., and Becker, K. (2007). Ultramicroscopy: three-dimensional visualization of neuronal networks in the whole mouse brain. *Nat. Methods* 4, 331–336.
- Ertürk, A., and Bradke, F. (2013). High-resolution imaging of entire organs by 3-dimensional imaging of solvent cleared organs (3DISCO). *Exp. Neurol.* 242, 57–64.
- Ertürk, A., Becker, K., Jährling, N., Mauch, C.P., Hojer, C.D., Egen, J.G., Hellal, F., Bradke, F., Sheng, M., and Dodt, H.-U. (2012a). Three-dimensional imaging of solvent-cleared organs using 3DISCO. *Nat. Protoc.* 7, 1983–1995.
- Famm, K., Litt, B., Tracey, K.J., Boyden, E.S., and Slaoui, M. (2013). Drug discovery: a jump-start for electroceuticals. *Nature* 496, 159–161.
- Femino, A.M., Fay, F.S., Fogarty, K., and Singer, R.H. (1998). Visualization of single RNA transcripts in situ. *Science* 280, 585–590.
- Gage, G.J., Kipke, D.R., and Shain, W. (2012). Whole animal perfusion fixation for rodents. *J. Vis. Exp.* 65, 3564.
- George, M.S., Sackeim, H.A., Rush, A.J., Marangell, L.B., Nahas, Z., Husain, M.M., Lisanby, S., Burt, T., Goldman, J., and Ballenger, J.C. (2000). Vagus nerve stimulation: a new tool for brain research and therapy. *Biol. Psychiatry* 47, 287–295.
- Hama, H., Kurokawa, H., Kawano, H., Ando, R., Shimogori, T., Noda, H., Fukami, K., Sakaue-Sawano, A., and Miyawaki, A. (2011). Scale: a chemical approach for fluorescence imaging and reconstruction of transparent mouse brain. *Nat. Neurosci.* 14, 1481–1488.

- Harmesen, M.M., and De Haard, H.J. (2007). Properties, production, and applications of camelid single-domain antibody fragments. *Appl. Microbiol. Biotechnol.* *77*, 13–22.
- Hoffman, A.S. (2002). Hydrogels for biomedical applications. *Adv. Drug Deliv. Rev.* *54*, 3–12.
- Jonkers, B.W., Sterk, J.C., and Wouterlood, F.G. (1984). Transcardial perfusion fixation of the CNS by means of a compressed-air-driven device. *J. Neurosci. Methods* *12*, 141–149.
- Ke, M.-T., Fujimoto, S., and Imai, T. (2013). SeeDB: a simple and morphology-preserving optical clearing agent for neuronal circuit reconstruction. *Nat. Neurosci.* *16*, 1154–1161.
- Kim, S.-Y., Chung, K., and Deisseroth, K. (2013). Light microscopy mapping of connections in the intact brain. *Trends Cogn. Sci.* *17*, 596–599.
- Kuwajima, T., Sitko, A.A., Bhansali, P., Jurgens, C., Guido, W., and Mason, C. (2013). ClearT: a detergent- and solvent-free clearing method for neuronal and non-neuronal tissue. *Development* *140*, 1364–1368.
- Leong, S.K., and Ling, E.A. (1990). Labelling neurons with fluorescent dyes administered via intravenous, subcutaneous or intraperitoneal route. *J. Neurosci. Methods* *32*, 15–23.
- Li, T., Bourgeois, J.P., Celli, S., Glacial, F., Le Sourd, A.M., Mecheri, S., Weksler, B., Romero, I., Couraud, P.O., Rougeon, F., and Lafaye, P. (2012). Cell-penetrating anti-GFAP VHH and corresponding fluorescent fusion protein VHH-GFP spontaneously cross the blood-brain barrier and specifically recognize astrocytes: application to brain imaging. *FASEB J.* *26*, 3969–3979.
- Lock, M., Alvira, M., Vandenbergh, L.H., Samanta, A., Toelen, J., Debyser, Z., and Wilson, J.M. (2010). Rapid, simple, and versatile manufacturing of recombinant adeno-associated viral vectors at scale. *Hum. Gene Ther.* *21*, 1259–1271.
- Lyubimova, A., Itzkovitz, S., Junker, J.P., Fan, Z.P., Wu, X., and van Oudenaarden, A. (2013). Single-molecule mRNA detection and counting in mammalian tissue. *Nat. Protoc.* *8*, 1743–1758.
- Moy, A.J., Wiersma, M.P., and Choi, B. (2013). Optical histology: a method to visualize microvasculature in thick tissue sections of mouse brain. *PLoS ONE* *8*, e53753.
- Pulicherla, N., Shen, S., Yadav, S., Debbink, K., Govindasamy, L., Agbandje-McKenna, M., and Asokan, A. (2011). Engineering liver-detargeted AAV9 vectors for cardiac and musculoskeletal gene transfer. *Mol. Ther.* *19*, 1070–1078.
- Raj, A., van den Bogaard, P., Rifkin, S.A., van Oudenaarden, A., and Tyagi, S. (2008). Imaging individual mRNA molecules using multiple singly labeled probes. *Nat. Methods* *5*, 877–879.
- Spalteholz, W. (1914). Über das Durchsichtigmachen von menschlichen und tierischen Präparaten (Leipzig: S. Hierzel).
- Steinke, H., and Wolff, W. (2001). A modified Spalteholz technique with preservation of the histology. *Ann. Anat.* *183*, 91–95.
- Susaki, E.A., Tainaka, K., Perrin, D., Kishino, F., Tawara, T., Watanabe, T.M., Yokoyama, C., Onoe, H., Eguchi, M., Yamaguchi, S., et al. (2014). Whole-brain imaging with single-cell resolution using chemical cocktails and computational analysis. *Cell* *157*, 726–739.
- Tomer, R., Ye, L., Hsueh, B., and Deisseroth, K. (2014). Advanced CLARITY for rapid and high-resolution imaging of intact tissues. *Nat. Protoc.* *9*, 1682–1697.
- Tseng, S.-J., Lee, Y.-H., Chen, Z.-H., Lin, H.-H., Lin, C.-Y., and Tang, S.-C. (2009). Integration of optical clearing and optical sectioning microscopy for three-dimensional imaging of natural biomaterial scaffolds in thin sections. *J. Biomed. Opt.* *14*, 044004.
- Zhang, M.D., Tortoriello, G., Hsueh, B., Tomer, R., Ye, L., Mitsios, N., Borgius, L., Grant, G., Kiehn, O., Watanabe, M., et al. (2014). Neuronal calcium-binding proteins 1/2 localize to dorsal root ganglia and excitatory spinal neurons and are regulated by nerve injury. *Proc. Natl. Acad. Sci. USA* *111*, E1149–E1158.

EXTENDED EXPERIMENTAL PROCEDURES

Animals

Wild-type mice (C57BL/6N and FVB/N, both males and females), *Thy1-YFP* mice (line H), and *Th-cre* (1Tmd/J) mice were used in the development and testing of novel clearing protocols and clearing reagents. *Thy1-YFP* mice were used to evaluate the maintenance of endogenous fluorescent signals throughout multi-week clearing steps and under long-term sample storage in RIMS. Periadolescent through adult wild-type rats (Long-Evans and Wistar, males and females) were used to optimize clearing protocols for larger tissue samples, and to depict the preservation of vasculature during lengthy perfusion-based clearing and antibody staining steps. For transcardial perfusion, subjects were deeply anesthetized with an overdose of Euthasol (100 mg/kg IP injection) prior to intracardiac perfusion first with heparinized PBS (10 U/ml heparin in 0.1 M PBS) containing 0.5% NaNO₂ and then with 4% PFA. For PACT, the brain and/or desired organs were excised and postfixed in 4% PFA for several hours prior to hydrogel monomer infusion and clearing steps. For PARS-based whole-body clearing, the intracardiac catheter was inserted into the left ventricle extending just beyond the aortic valve, stabilized inside the aorta with a loose loop of suture thread. For PARS-based whole-brain clearing, the descending aorta was ligated with a microclamp.

For experiments involving the visualization of AAV9-CAG-eGFP transduced cells, young adult female C57Bl/6 mice were injected with virus via the retro-orbital sinus, and following a 6 month delay for viral transduction and eGFP expression, mice were euthanized for PACT and PARS studies.

Ethics Statement

Animal husbandry and all experimental procedures involving mice and rats were approved by the Institutional Animal Care and Use Committee (IACUC) and by the Office of Laboratory Animal Resources at the California Institute of Technology.

AAV Production and Systemic Delivery

By injecting mice with adeno-associated viral vectors carrying fluorescently labeled transgenes, we were able to observe the compatibility of PARS processing and RIMS mounting with more sparse, localized fluorescent labeling than that which is driven by the *Thy1* promoter (Figures 5A–5C versus Figures 5D and 5E). Sparse labeling of specific neuron types and glia as well as localized eGFP expression in distinct organs (e.g., liver and hippocampus Figures 5D and 5E) was clearly visible. Single stranded ssAAV-CAG-eGFP vectors packaged into AAV9 or the AAV9 variant capsid, AAV9BD1, was generated and purified as described (Lock et al., 2010). The AAV9BD1 capsid was modified from AAV9 (U. Penn) with the following mutations (VP1 numbering): (1) An N498Y mutation was made to reduce liver transduction (Pulicherla et al., 2011), (2) the amino acid sequence AAADSPAHPHS (Chen et al., 2009) was inserted between AA588–589, and (3) a Y731F mutation was made (Pulicherla et al., 2011). 1×10^{12} vector genomes (vg) of either virus was delivered intravenously into young adult female C57Bl/6 mice via the retro-orbital sinus and the mice were euthanized 6 months later for assessment of native eGFP fluorescence by PARS. All imaging of PARS brain and liver tissue from AAV9-injected mice was performed after 2 weeks tissue storage in RIMS.

Selection of PACT and PARS Reagents

To screen different hydrogel monomer formulations and clearing conditions, several adult C57 and *Thy-1* eYFP mice (Jackson) were anesthetized with an overdose of Euthasol (100 mg/kg, IP injection) and transcardially perfused first with PBS containing 0.5% NaNO₂ and 10 U/ml heparin, and then 4% paraformaldehyde (PFA, in 0.1 M PBS, pH 7.5). The excised whole brains were sliced into 1 mm and 3 mm sagittal sections and coronal sections, postfixed in 4% PFA at room temperature for 2–6 hours (postfixing whole brain and sections at 4 °C overnight is also a valid option), and then sections were incubated at 4 °C overnight in A2P0 (2% acrylamide and 0% paraformaldehyde in PBS), A4P0 (4% acrylamide and 0% paraformaldehyde in PBS), or A4P4 (4% acrylamide and 4% paraformaldehyde in PBS) hydrogel monomer solution, each containing 0.25% photoinitiator 2,2'-Azobis[2-(2-imidazolin-2-yl)propane] dihydrochloride (VA-044, Wako Chemicals USA). While still submerged in hydrogel monomer, the hydrogel-infused samples were degassed by bubbling nitrogen through the sample-hydrogel solution in the vacutainer or 5 ml Eppendorf tubes for 1 min. It should be noted that we experimented with several, more rigorous methods of replacing oxygen atmosphere with an inert gas, as was deemed necessary in the original and advanced CLARITY protocols (Chung et al., 2013; Tomer et al., 2014) (e.g., 1. Placing the vacutainer containing the sample on ice; 2. Degassing the vacutainer with the house vacuum line while gently vortexing for several minutes; 3. Removing the sample from ice and bubbling nitrogen through the hydrogel monomer solution for several minutes; 4. Repeating steps 1–3 several times). However, we found that the brief 1 min exchange of oxygen for nitrogen supported adequate polymerization: residual oxygen may have hampered the complete hybridization between tissue and acrylamide monomers; however, our tissue-hydrogel matrix was sufficient for preserving tissue architecture and protein content. To polymerize the hydrogel-tissue matrix, the samples were transferred to a 37 °C waterbath or heating block and incubated for 2–3 hr at this elevated temperature. The polymerized samples were washed briefly with PBS (0.1 M PBS, pH 7.5; all PBS wash steps) to remove excess hydrogel, transferred to 50 ml conical tubes, and incubated for 2–5 days at 37 °C with shaking in either PBS, 0.1% Triton X-100 in PBS, or a clearing solution: 4% SDS, 8% SDS, 20% SDS, or 10% Deoxycholate, all prepared in 0.1 M PBS, pH 7.5. Images of 3 mm brain sections were taken at 24 hr and 48 hr (Figure 1A) to show the trade-off between greater tissue swelling for tissue-hydrogel matrices prepared with low PFA concentrations, and slower tissue clearing for tissue-hydrogel matrices prepared with high PFA

(and acrylamide) concentrations; the A4P0 hydrogel formulation was selected for general use in subsequent PACT and PARS experiments. A 72 hr incubation of brain sections in the 8% SDS clearing solution resulted in superior tissue clearing (Figure S1A), and so the 8% clearing solution was selected for subsequent PACT and PARS experiments. Regarding clearing time, this parameter must be optimized in a case-specific manner. 24 hr clearing may be sufficient for small tissue samples or highly porous tissue, while larger, highly myelinated, or dense tissue sections and whole organs may require > 96 hr. Care must be taken to not overclear the samples and also to check periodically for excessive swelling if samples are to be stored long term since swelling does contribute to hydrogel softening and disintegration in the long run, risking sample loss. This is accelerated by elevated temperature and mechanical stress during sample preparation and handling. Gentle treatment of the tissue-hydrogel samples and the addition of antimicrobial agents to incubation solutions allow the hydrogel to remain stable for up to two weeks. Also, we found that an additional round of tissue cross-linking with 1%–2% PFA, or of tissue-hydrogel re-polymerization after clearing, was beneficial to counteracting both tissue expansion in mounting media and tissue disintegration.

PACT Immunohistochemistry

To immunostain PACT-processed tissue, cleared samples were washed with 4–5 changes of PBS over 1 day to remove residual SDS. Then, the samples were incubated with primary antibodies (1:200–400) in PBS containing 2% normal donkey serum, 0.1% Triton X-100 and 0.01% sodium azide at room temperature with shaking for 3–7 days. Six A4P0-polymerized and six A4P4-polymerized 3-mm sagittal sections were removed from these antibody incubations at 24 hr, 48 hr, and 72 hr in order to measure IgG penetration depth in cleared tissue (see Figure 1B). For remaining sections, unbound primary antibody was removed via washing sections in 4–5 PBS buffer exchanges over the course of one day. Then, samples were incubated with secondary antibodies (Fab fragment secondary antibodies are preferred, 1:200–400, in PBS containing 2% normal donkey serum, 0.1% Triton X-100 and 0.01% sodium azide) at room temperature with shaking for 2–5 days.

After washing with 4–5 changes of PBS over 1 day, the samples were incubated in RIMS solution (40 g of Sigma D2158 (Histodenz) in 30 ml of 0.02 M phosphate buffer with 0.01% sodium azide, pH to 7.5 with NaOH—which results in a final concentration of 88% Histodenz w/v) at room temperature until they became transparent. During long incubations (>4 days) of tissue in antibody, small-molecule stains, or RIMS, the solution was exchanged for fresh halfway through the incubation. As an extra precaution and to prevent bacterial growth, tissues may be transferred to fresh 50 ml conical tubes or staining jars with every buffer exchange. It is suggested that RIMS incubations and mounting be performed in a clean environment—either in a hood, or by decanting RIMS into a fresh conical over flame to minimize bacterial contamination.

The primary antibodies used for passive staining were chicken anti-tyrosine hydroxylase (TH) IgY, chicken anti-glial fibrillary acidic protein (GFAP) IgY (Aves Labs, Tigard, OR), rabbit anti-ionized calcium-binding adaptor molecule 1 (Iba1) IgG (Biocare medical, Concord, CA), rabbit anti-integrin b4, b5 IgG, and rabbit anti-beta tubulin IgG (Santa Cruz Biotechnology, Dallas, Texas). An AlexaFluor 647-conjugated donkey anti-mouse IgG (Jackson ImmunoResearch, West Grove, PA) was used for the antibody penetration experiment (Figure 1B). Nissl staining was performed with NeuroTrace 530 / 615 Red Fluorescent Nissl Stain (1:50 in PBS, Life Technologies, Grand Island, NY; samples were incubated at RT overnight and then washed in PBS prior to mounting. For small molecule staining with acridine orange, samples were placed in a 100 µg/ml solution of acridine orange for 10 min, followed by washout in PBS for one hour. The tissues were then placed in RIMS solution for 4 hr prior to imaging. All steps were performed at room temperature.

PARS Chamber Design

To perform PARS, a simple apparatus was needed to perfuse and recirculate PACT reagents through the circulatory systems for several days-to-weeks. Using the traditional cardiac perfusion fixation technique (Gage et al., 2012; Jonkers et al., 1984) as a delivery method, we devised a PARS chamber that consisted of the following components: 1) a feeding needle catheter placed within the left ventricle of the subject, 2) a perfusate collection well (pipette box) to catch recirculating reagents that exit the vasculature through a lesioned right atrium, and 3) catheter tube that transfers recirculating reagents from the collection well back into subject vasculature via its passage through a peristaltic pump (Figure S4A). To confirm that this set-up was functional for whole-organism clearing, several different detergents including SDS at several different percentages, sodium lauryl sarcosine, and sodium deoxycholate, at various concentrations, were continuously perfused through whole mice and rats via the carotid artery for up to 2 weeks. As in PACT (Figure S1A), only SDS could effectively render tissue transparent for optical imaging. Likewise, when delivered using the PARS chamber set-up, 8% SDS could efficiently solvate lipids deep in tissue and accomplish uniform clearing of large tissue samples. Thus, the PARS chamber set-up was adopted for subsequent PARS experiments.

PARS Clearing and Staining

For transcardial perfusion fixation of adult mice or rats, a feeding needle was inserted through the left ventricle and into the aorta, and loosely sutured in place to the vessel at the level of the aortic arch. Following perfusion with PBS and 4% PFA, as summarized for PACT, the fixed whole rodents were transferred into a custom-built perfusion chamber where the solutions inside the chamber are perfused into the rodent and recirculated via a peristaltic pump. The rodent was postfixed with 4% PFA through the same feeding needle into the aorta at a flow rate of 1 ml/min for 1–2 hr at room temperature. For clearing of rat brain and spinal cord, we systematically ligated the arterial circulation leaving the carotid arteries intact and removed tissue not directly perfused

by these vessels. To prevent excess PFA-crosslinked polyacrylamide from occluding the vasculature, we first perfused PBS (0.1 M PBS, pH 7.5; all PBS wash steps) for 2 hr at RT to wash out the residual PFA and we infused 4% acrylamide (A4P0) in PBS at RT overnight. The next day, we again perfused PBS to remove any remaining PFA/acrylamide polymers/monomers in the vasculature. Before polymerization and without disconnecting perfusion lines, we placed the perfusion chamber into a ziplock bag and infused nitrogen gas into the perfusion chamber through a separate connection to degas the sample. The polymerization process was initiated by adding 200 ml of 0.25% VA-044 initiator with PBS and submerging the degassed perfusion chamber in a 37–42 °C water bath for 2–3 hr. A lead weight was placed on top of the perfusion chamber to prevent it from tipping over. After polymerization, the solution was replaced with 8% SDS in 0.1 M PBS, pH 7.5 clearing buffer, and the mouse/rat was perfused for up to 2 weeks. For PARS IHC, the cleared mouse/rat was first perfused with 8 buffer changes of 200 ml PBS over a 2 day period to remove the residual SDS. Then, using the same antibody formulations described in the PACT protocol, a 3 day perfusion with a primary antibody cocktail, 1-day perfusion with PBS wash, a 3 day perfusion with the secondary antibody cocktail, and a 1 day PBS wash was conducted in order to stain the organs of the cleared mouse/rat.

PARS-CSF Methodology for Brain and Spinal Cord Clearing

For applications restricted to brain and spinal cord mapping, we developed a within-skull PARS strategy that grants thorough clearing of the whole-brain and whole-spinal cord by direct infusion of hydrogel monomers and clearing reagents into the CSF via an intracranial brain shunt. Under specific circumstances (e.g., the pre-existing availability of a guide cannula in the subject from an *in vivo* pharmacological, neurobiological, or optogenetic study), PARS-CSF would permit whole-brain clearing and histology that is automatically optimized for the region near the existing cannula, and that requires less time and reagents as the equivalent whole-organ PACT and PARS procedures.

Herein, we validated two routes for intracranial delivery of PACT reagents. To clear the spinal cord, a cannula may be lowered through the skull (by drilling a hole in the region of interest and using tweezers to create an opening in the dura), to the level of the subarachnoid space, directly above the dorsal inferior colliculus, (see [Figure 3A](#), right). The rat spinal cord sample (see [Figure 3B](#), right) could be cleared when PARS-CSF was conducted at elevated temperatures and for a longer period of clearing. To clear the whole brain, the cannula may be lowered through the skull, penetrating the dura, and placed in the region directly above the olfactory bulb (see [Figure 3B](#), left). The cannula (21G blunted needle BD) is cemented in-place on the skull surface using dental acrylic (C&B-Metabond, Parkell). The PARS procedure was then applied to this intracranial preparation: the catheter tubing was connected to the subdural cannula as opposed to the cardiac feeding tube, and all PACT reagents were infused at 1 ml/min using the same order and timeframe as in PARS. For whole-brain clearing, the subject was transcardial-perfusion fixed and decapitated, with only the head transferred to the PARS chamber and connected to the infusion lines ([Figure S4A](#)). The pipette box and catheter lines were pre-filled with 4% acrylamide monomer solution (A4P0), the tubing was connected to the cannula, and A4P0 was intracranially infused at a 1 ml/min flow rate overnight at room temperature ([Figure S4A](#), left). After flushing the brain of unbound PFA and acrylamide monomers (2 hr infusion of PBS), which was critical to ensure that the vasculature remained unpolymerized, the whole brain was degassed via transferring the PARS chamber into a ziplock bag and placing the chamber under an inert atmosphere (N₂) for two minutes ([Figure S4A](#), right). The bagged-PARS chamber was then transferred to a 37–42°C water bath, and degassed PBS supplemented with the thermal initiator was infused through the brain for the entire 2–3 hr incubation. After formation of this whole-brain-hydrogel matrix, in-skull tissue clearing was accomplished via constant perfusion recirculation of 8% SDS through the cannula for 4 days, with the PARS chamber remaining in the 37–42°C water bath for the entire process. Finally, after extensive PBS washing (2–3 days), the catheter lines were disconnected, and the brain was removed, sectioned, and mounted in RIMS for imaging ([Figure 3B](#)).

Using mice that were IV-injected with AAV9-eGFP, the PARS-CSF procedure for whole-organ clearing was validated with respect to the following conditions: (1) only limited bias in how well regions clear relative to the cannula placement, (2) no structural damage in regions near the cannula due excessive fluid pressure, either from too high flow rate or inadequate drainage of perfused liquids, causing high intracranial pressure, (3) preservation of subcellular structural morphology, and (4) good visualization of sparsely labeled cell populations and fluorescence. It may have particular relevance to scientists performing research that already involves the use of intracerebroventricular (ICV) cannulated mouse or rat subjects and that requires postmortem brain histology for each subject.

Antibody Penetration

Four transcardially perfused and 4% PFA postfixed adult mouse (4–12 weeks old) brains were cut into 2 mm sagittal slices, and these slices were PACT processed. Specifically, one half of each PFA-fixed brain was hybridized with A4P4 hydrogel, while the other half was hybridized in A4P0 hydrogel. All the samples were passively cleared with 8% SDS in PBS, as described in the PACT protocol, and the residual SDS was removed by PBS washing for 1 day. The samples were then incubated in primary antibody cocktails (donkey anti-mouse-IgG antibody, 1:200, in PBS containing 2% normal donkey serum, 0.1% Triton X-100 and 0.01% sodium azide) for a range of time-periods, spanning 24–72 hr. Samples were then washed with 4–5 buffer exchanges of 0.1 M PBS over 1 day and mounted in RIMS solution. Images were taken with a Zeiss LSM 780 confocal microscope using the W Plan-Apochromat 20×/1.0 DIC M27 (working distance 1.8 mm). The depth of antibody penetration ([Figure 1B](#)) was outlined on y-z projected images using Fiji ([Schindelin et al., 2012](#)) with Reslice and Z project plugins.

RIMS for PACT and PARS Samples

As a final step in tissue preparation for imaging, sample mounting comprises immersing the tissue section in a medium that will help to align the refractive indices of the objective, lens immersion media, and tissue, which confers higher-resolution and -imaging depth. In order to circumvent the use of FocusClear, a prohibitively expensive reagent, in mounting our PACT and PARS samples, we elected to formulate our own mounting solution alternative.

Based on the principles of tissue optical clearing, we rationally screened two major groups of chemicals (sugar alcohols and radiocontrast agents) that have the following desirable characteristics of an optical clearing agent: high water solubility, low viscosity, high density, low osmolarity, low autofluorescence, nonfluorophore quenching, biocompatible, low cost. We identified sorbitol, a sugar alcohol that is affordable and widely available. At 70–80% (w/v) solution, sorbitol can effectively clear 200 μm thick uncleared and up to 1 mm thick PACT-cleared brain sections with little quenching of fluorescence. The formulation (termed sRIMS, see below for description) was later optimized to include 0.02–0.05 M phosphate buffer (pH maintenance), 0.1% tween-20 (enhances tissue penetration), and sodium azide (preservative to inhibit bacterial growth). In addition to sugar alcohols, we also looked at radiocontrast agents, especially intravascularly delivered non-ionic iodinated contrast agents (also licensed for use as density gradient media) as their physical and chemical properties closely match that of an ideal refractive index matching media. Based on cost and availability, we tested iodixanol (Optiprep) and its monomer iohexol (Nycodenz, also available as Histodenz, a derivative of iohexol) and found iohexol to be superior than sorbitol in index matching much larger PARS-cleared samples.

Next, we conducted a side-by-side comparison (see Figure S3A) between commonly used/commercially available mounting options: 80–90% glycerol and FocusClear, and our most promising mounting media candidates: sRIMS and RIMS, a mounting media optimized for our imaging set-up with standard confocal microscopy. RIMS solution was prepared via dissolving 40 g of Histodenz (Sigma D2158) in 0.02 M phosphate buffer with 0.01% sodium azide for a total volume of 30 ml, pH to 7.5 with NaOH, which results in a final concentration of 88% Histodenz (w/v) with RI = 1.46 (used throughout this work unless otherwise noted). Estimated cost to produce is \$3/ml while FocusClear is \$36/ml. We note that the refractive index (RI) of RIMS may be adjusted to match the specific tissue/imaging system: it is expected that the RIMS RI may range from 1.38 (30% Histodenz w/v) to 1.48 (95% Histodenz w/v) in order to obtain optimal sample resolution. Light transmittance in RIMS (Figure S3B) was measured with a Reichert AR200 Refractometer. For RIMS mounting, samples were first submerged in RIMS at room temperature until they become transparent. During this period, the cleared tissue initially shrinks for the first few hours (see Figure S3D). Continued incubation in RIMS will lead to gradual tissue expansion over time until RIMS has fully penetrated the tissue (see Figures 4C and S5A); we observed that our largest samples (e.g., rat whole brain) became transparent within one week of RIMS-immersion, after which their expansion ceased. We were able to limit tissue expansion, however, by postfixing the cleared and stained samples in 4% PFA for 1–2 hr at room temperature (small samples) or up to overnight (large samples) before proceeding to RIMS incubation (see Figure 4C, right box; Figure S5A, lower right box). Although postfixing PARS tissue curtailed gradual tissue volume expansion, the additional crosslinking also precipitated a slight decrease in tissue transparency (Figure S5A). Fluorescence intensity, cell phenotyping, or resolvable depth of imaging were not adversely affected, however.

sRIMS: A Cost-Effective Sorbitol-Based Alternative to RIMS

70% sorbitol (w/v) (Sigma S1876) in 0.02 M phosphate buffer with 0.01% sodium azide, pH to 7.5 with NaOH; net cost of \$0.2/ml.

While RIMS outperformed sRIMS in our hands in terms of resolvable imaging depth, sorbitol is a commonly available chemical across scientific laboratories, and thus offers a convenient, cost-effective and superior alternative to glycerol-based mounting solutions.

Vasculature Preservation

Rats were transcardially perfused with heparinized PBS, 4% PFA, and lastly additional PBS wash. Then, before any hydrogel monomer infusion or clearing as in PARS, the rat was perfused via its intra-aortic catheter with 100 ml Atto 488-conjugated anti-GFAP nanobody (1:100 in PBS) at room temperature overnight. The GFAP nanobody was prepared according to published methods (Li et al., 2012). It was conjugated to Atto 488 fluorescent dye prior to use. The brain was removed from the skull and incubated in 4% PFA at 4°C overnight to crosslink the nanobody. The brain was then cut into 1 mm coronal slices processed according to standard PACT protocols, including hydrogel monomer infusion, hybridization, and passive sample clearing in 8% SDS in 0.1 M PBS, pH 7.5 at 37°C for 3 days. Cleared samples were incubated in RIMS solution for one day and mounted in RIMS solution for imaging. Images were taken using Zeiss LSM 780 confocal microscope with LD LCI Plan-Apochromat 25x/0.8 Imm Corr DIC M27 multi-immersion objective.

The above methods were repeated in mice for the labeling of vasculature with Alexa Fluor 647-conjugated anti-mouse IgG. Briefly, 4% PFA-fixed mice were transcardially perfused with Alexa Fluor 647-conjugated anti-mouse IgG overnight using the same intra-aortic catheter that was installed for 4% PFA fixation. The brain was excised, post-fixed in 4% PFA at 4°C overnight, sectioned into 1 mm coronal slices and PACT cleared in 8% SDS in 0.1 M PBS, pH 7.5 at 37°C for 3 days. Cleared samples were incubated in RIMS solution for one day and mounted in RIMS solution for imaging.

Sliced Tissue Expansion and Weight Gain Measurement

PFA-fixed adult mouse (4–12 weeks old) brain was cut into six 1-mm-thick coronal slices. Slices from one half of the brain were stored in PBS, while slices from the other half of the brain were PACT-cleared for 4 days. Slices were weighed and imaged with a

conventional camera before and after clearing. The size of the slices was outlined and calculated using Image J. The tissue expansion and weight gain were determined by calculating the change in size and weight of slices before and after clearing (Figure 1E), and normalizing them to the pre-PACT measurements.

Protein Loss Measurement

The percentage of protein loss for each sample (Figures 1C and 4E) was obtained by measuring the amount of total protein in the clearing solutions collected from PACT or PARS clearing with NanoDrop blanked with respective solutions, and normalized to the weight of the mouse (for PARS) or the slices (for PACT) before clearing.

Whole-Brain Tissue Morphology Preservation and Quantification

To observe the effect of PARS processing and RIMS mounting on brain volume, PFA-fixed adult mouse brains were either immediately extracted (uncleared control) or PARS-processed; and then brains from these two groups were treated according to one of the following conditions: incubated in PBS for 1 day, incubated in PBS for 1 week, mounted in RIMS for 1 day, mounted in RIMS for 2 weeks, or postfixed and mounted in RIMS for 2 weeks. Cleared and uncleared brains from all conditions were then photographed to estimate their relative size change (Figure 4C), cut into sections to visualize clearing depth (Figure S5A), slide-mounted, and imaged via confocal microscopy in order to evaluate gross changes in tissue architecture (e.g., morphological deformations of major brain regions, structure integrity of ventricles and vasculature) (Figure S5B). The percentage of protein loss for each sample (Figures 1C and 4E) was obtained by measuring via NanoDrop the protein concentration of clearing solution aliquots that were collected after PACT or PARS-processing of tissue. The net protein loss could then be estimated based on this concentration and the known total volume of clearing solution used during processing. The amount of protein lost by each sample was normalized to the weight of the mouse (for PARS) or the tissue slice (for PACT) before clearing so that protein losses across samples and across tissue processing conditions could be compared.

Single-Molecule RNA FISH

Tissue samples were adhered to aminosilane-treated coverslips by dehydrating for 1 hr under light vacuum. Samples were permeabilized prior to hybridization according to the following protocol: First, samples were washed twice in 100% ethanol for 10 min at room temperature. Next samples were washed in 95% ethanol for 10 min at room temperature. Samples were then incubated in 70% ethanol for 2 hr at 4°C. After incubation, tissue was placed in a 0.5% sodium borohydride (w/v) 70% ethanol solution for 10 min at room temperature. Finally, the tissue was rehydrated with 3 washes of PBS.

Hybridizations were performed overnight at 37°C in a hybridization buffer composed of 10% dextran sulfate (w/v, Sigma D8906), 10% formamide (v/v), 2× SSC containing 1 nM per each of 24 Alexa 594-labeled 20-mer oligo probes toward β -actin. The next day samples were washed in 30% Formamide 2× SSC at room temperature for 30 min followed by 4 washes with 2× SSC. After washing sample was mounted between two coverslips with Slowfade Gold + DAPI (Life S36938). Samples were imaged on a Nikon Ti Eclipse microscope with an Andor Ikon-M camera and a 60×/1.4NA Plan Apo λ objective with an additional 1.5× magnification. Images were acquired as z stacks with a 0.5 μ m step size over 30 μ m. Samples were excited by a 589 nm (SDL-589-XXXT), 532 nm (SDL-532-200TG) and 405 nm (SDL-405-LM-030) lasers manufactured by Shanghai Dream Laser.

The smFISH images (Figure 2) were analyzed using image analysis scripts written in MATLAB. To determine the average background of the sample, the images were median filtered using a 50 × 50 pixel kernel and the average pixel intensity of the center 200 × 200 pixel sub-image was used as the average background value of the image. The smFISH dots were found by applying a Laplacian of Gaussian filter, thresholding the image based on the average background value and comparing the resulting image with a dilated image to find local maxima. The error bars were calculated using the standard deviation of the resulting measurements.

Human Tissue Biopsy Preparation

Human basal cell carcinoma skin tissue samples were obtained from patients undergoing excision of their cancers after appropriate informed consent and under approval of UCLA IRB #12-01195. Tissue samples were obtained from sections of tumors not necessary for diagnostic or margin control purposes and varied in size depending on the size of the original skin cancer.

Biopsied tumor samples were processed utilizing the PACT methodology as described for rodent tissue, using 4% acrylamide solution (A4P0) to generate hydrogel support matrix for fixed tissue. Polymerized tissue-hydrogel matrices were then passively cleared for 2–7 days (i.e., depending on tissue thickness) in 8% SDS at 37°C. In general, a 3-mm-thick human skin section could be rendered transparent within 3–4 days.

PACT-processed samples were immunolabeled with anti-pan-cytokeratin (AE1/AE3) Alexa Fluor 488 primary antibodies (eBiosciences) at 1:100 dilution for two days followed by a 1 day wash in PBS. All labeling and wash steps were performed at room temperature, and final PACT-processed biopsy samples were mounted in RIMS. Imaging was performed on a Zeiss 780 confocal microscope with a LD LCI Plan-Apochromat 25×/0.8 N.A. multi-immersion objective.

Despite testing a range of clearing times (2–7 days in 8% SDS) for tissue-hydrogel samples, the subcutaneous layer (consisting primarily of adipocytes) resisted consistent clearing (yellow tissue, Figure S2A) due to incomplete micelle solvation of all the packed lipids in adipocytes.

Scanning Electron Microscopy

Samples were imaged on an FEI Quanta 200F environmental scanning electron microscope (ESEM) in ESEM mode. Thin slices of PACT-processed brain tissues were placed on the sample holder in the chamber and imaged at a voltage of 5 kV and working distance between 7.7–8.3 mm with a spot size of 3 or 4 using the gaseous secondary electron detector (GSED). Please note that stretching during cutting/SEM process will make the pores of tissue-hydrogel hybrid larger. The actual effective pore size of the SEM images should be smaller than we present here.

Quantification Methods

Mean nearest neighbor distance (NND): 1-mm-thick coronal slices were stained with DAPI and imaged w/ the 10× 0.45 N.A. Plan-Apochromat objective. Twenty-four 3- μ m-thick images were taken from different regions of the cortex thalamus and striatum. A 30 pixel rolling ball radius subtraction filter was used to remove the background. Individual images are thresholded and converted into binaries. A binary watershed segmentation was applied to divide cells that are clustered together. The resulting images were quantified with the analyzing particles option on ImageJ. The centroid of each cell was identified in the measurement, and the NND's were calculated by applying the "nnd" plugin on imageJ.

GFP size quantification: 1-mm-thick coronal slices of AAV9-eGFP IV injected mouse brain were imaged with the 5× 0.25N.A. Fluar objective. A maximum projection of the Z-stack was used for quantification. The area of each GFP positive neuron was isolated and quantified with the analyzing particles option on ImageJ.

Both nearest neighbor distance measurements and GFP size calculations were performed for three brain regions: cortex, striatum, and thalamus; in uncleared, PARS cleared, and PARS cleared then postfixated mouse brain slices (see [Figure S5A](#) for representative brain slices and [Figure S5B](#) for data results). The mean cell size and mean NND for all counted cells were computed for each region, and data were analyzed for statistically significant differences in cell size or in NND between regions.

Fluorescence Microscopy

Cleared tissue samples were incubated in RIMS solution for one day. The samples were then mounted in the respective solutions using 7.0 mm or 3.0 mm spacers (iSpacer, SunJin Lab), or 0.5 mm or 2.5 mm spacers (Silicone Isolator, Electron Microscopy Sciences, PA) with coverglasses. Coverslipped samples were stored at room temperature and shielded from light prior to imaging. Of note, most fluorescent images and initial sample visualization were performed on a conventional confocal microscope (Zeiss LSM 780) with either the Fluar 5×/0.25 M27 objective (working distance 12.5 mm), Plan-Apochromat 10×/0.45 M27 objective (working distance 2.0 mm), LD SC Plan-Apochromat 20×/1.0 Corr M32 85 mm scale-immersion objective (working distance 5.6 mm), or LD LCI Plan-Apochromat 25×/0.8 Imm Corr DIC M27 multi-immersion objective (working distance 0.57 mm). The only exceptions were for smFISH experiments, which used a Nikon Ti Eclipse microscope with an Andor Ikon-M camera and a 60×/1.4NA Plan Apo objective, and for the acquisition of images presented in [Figure 5B](#), wherein samples were imaged by Leica Microsystems using a Leica TCS SP8 two-photon microscope with the Leica HC FLUOTAR L 25×/1.00 IMM CORR objective (working distance 6.0 mm). Image reconstructions were performed using Imaris imaging software (Bitplane). After imaging, samples were embedded in RIMS at room temperature and protected from light for storage.

SUPPLEMENTAL REFERENCES

- Chen, Y.H., Chang, M., and Davidson, B.L. (2009). Molecular signatures of disease brain endothelia provide new sites for CNS-directed enzyme therapy. *Nat. Med.* 15, 1215–1218.
- Ertürk, A., Mauch, C.P., Hellal, F., Förstner, F., Keck, T., Becker, K., Jährling, N., Steffens, H., Richter, M., Hübener, M., et al. (2012). Three-dimensional imaging of the unsectioned adult spinal cord to assess axon regeneration and glial responses after injury. *Nat. Med.* 18, 166–171.
- Jung, Y., Ng, J.H., Keating, C.P., Senthil-Kumar, P., Zhao, J., Randolph, M.A., Winograd, J.M., and Evans, C.L. (2014). Comprehensive evaluation of peripheral nerve regeneration in the acute healing phase using tissue clearing and optical microscopy in a rodent model. *PLoS ONE* 9, e94054.
- Ke, M.T., and Imai, T. (2014). Optical clearing of fixed brain samples using SeeDB. *Curr. Protoc. Neurosci.* 66, 22.
- Lubeck, E., Coskun, A.F., Zhiyentayev, T., Ahmad, M., and Cai, L. (2014). Single-cell in situ RNA profiling by sequential hybridization. *Nat. Methods* 11, 360–361.
- Perruchini, C., Pecorari, F., Bourgeois, J.P., Duyckaerts, C., Rougeon, F., and Lafaye, P. (2009). Llama VHH antibody fragments against GFAP: better diffusion in fixed tissues than classical monoclonal antibodies. *Acta Neuropathol.* 118, 685–695.
- Schindelin, J., Arganda-Carreras, I., Frise, E., Kaynig, V., Longair, M., Pietzsch, T., Preibisch, S., Rueden, C., Saalfeld, S., Schmid, B., et al. (2012). Fiji: an open-source platform for biological-image analysis. *Nat. Methods* 9, 676–682.

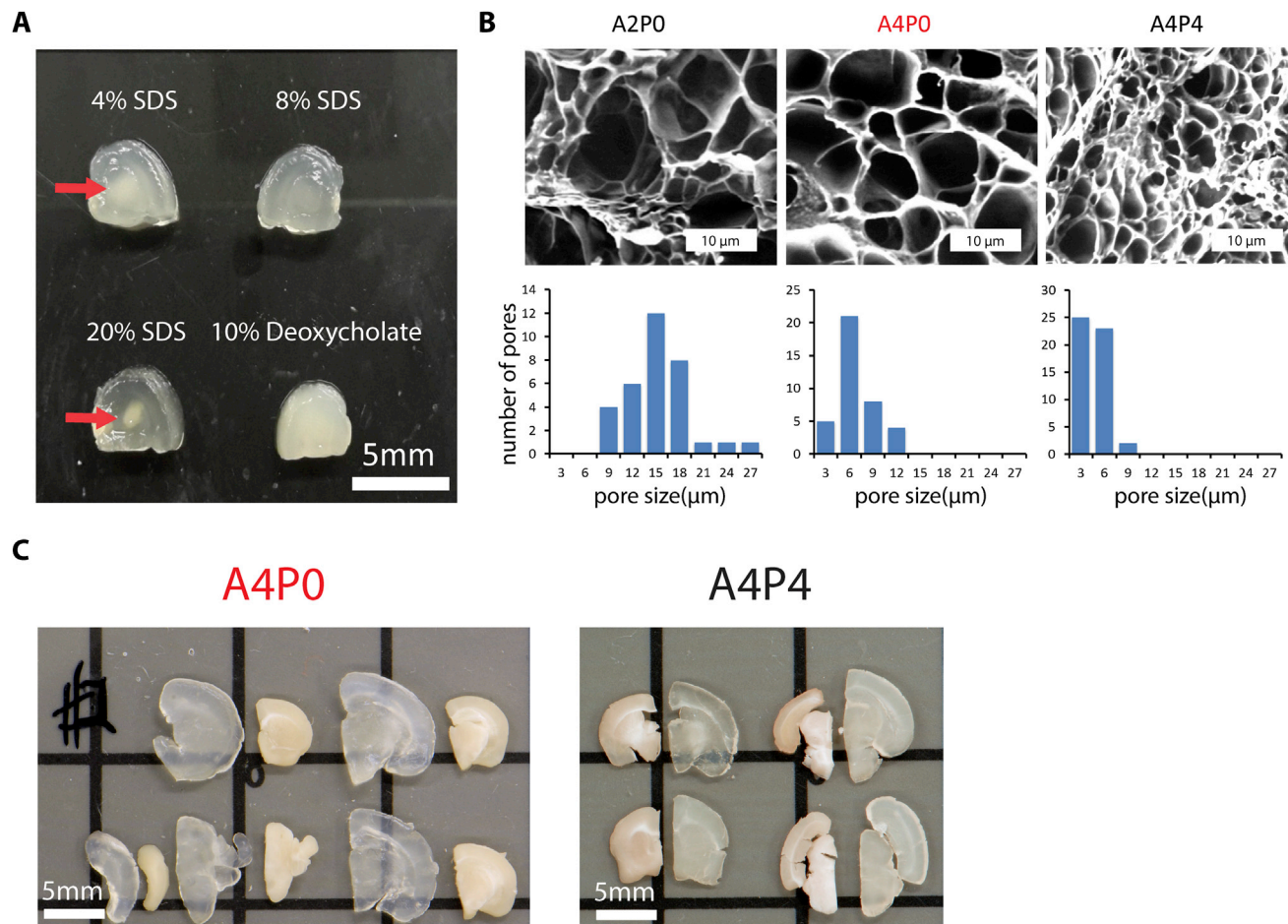


Figure S1. PACT-Cleared A4P0 Tissue-Hydrogel Hybrid Using 8% SDS Shows Optimal Optical Transparency, Related to Figure 1, 3, and 4, and Table S2

(A–C) All samples were PACT cleared for 3 days. (A) Comparison of optical transparency of 3 mm mouse brain coronal blocks PACT cleared using different percentage of SDS and 10% sodium deoxycholate (arrows indicate incomplete clearing). (B) Scanning Electron Microscopy (SEM) images showing the pores of tissue hybridized with different hydrogel percentages; the histograms below indicate the distribution of the pore size for each condition. (C) Compared to A4P4, A4P0 tissue-hydrogel hybrids show greater tissue expansion and optical transparency (1 mm mouse brain slices). Samples for (B) and (C) were PACT cleared in 8% SDS. Images for (A) and (C) were taken using bright field camera.

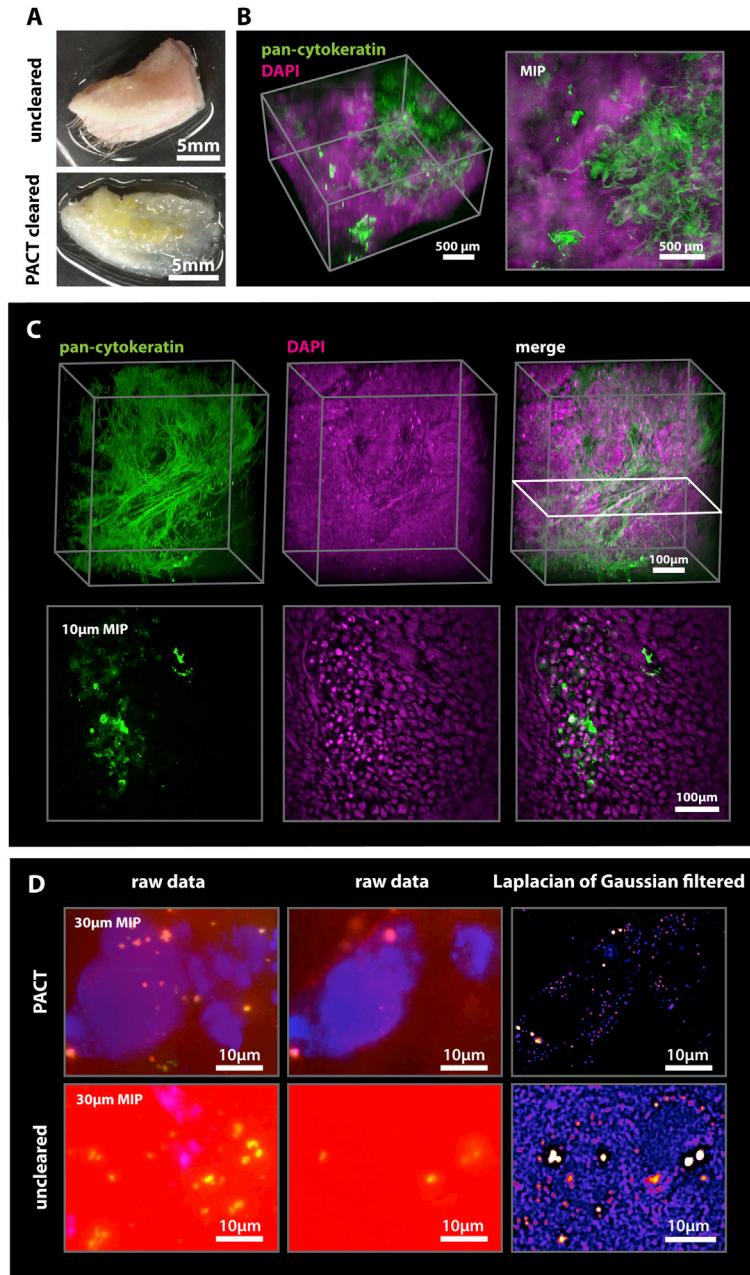


Figure S2. PACT Samples Are Compatible with Gross Tissue Pathology and Fine Transcriptional Analysis, Related to Figures 1 and 2

(A–C) A 3-mm-thick section of a human basal cell carcinoma (BCC) tissue biopsy was cleared with PACT, immunolabeled with anti-pan-cytokeratin (AE1/AE3) antibody, and counter-stained with DAPI. (A) Photographs of uncleared (top) and cleared 3-mm-thick section (bottom) of human basal cell carcinoma (BCC) tissue biopsy (scale bars, 5 mm). (B) Low-magnification (5 \times) ($z = 1.5$ mm) and (C) high-magnification (25 \times) ($z = 500$ μ m) 3D rendering and maximum intensity projections showing locations of AE1/AE3 positive cells and keratin filament remnants (green) of apoptotic tissue with respect to all cells (magenta) of the region. (scale bars, 500 μ m and 100 μ m).

(D) Background differences between preprocessed (except background subtraction on DAPI channel) (left and middle) and postprocessed (right) images of PACT cleared (top) and uncleared (bottom) smFISH brain slices. Left: 30 μ m maximum intensity projection (MIP). Middle: single 0.5 μ m image at a depth of 3 μ m. Right: Laplacian of Gaussian (LoG) filtered, contrast adjusted image from middle.

All images were processed with identical contrast threshold and LoG filtering parameters. Objectives used for confocal imaging: (B and C) Zeiss 5 \times 0.25 N.A. Fluor objective and the LD LCI Plan-Apochromat 25 \times /0.8 N.A. multi-immersion objective; (D) smFISH Samples imaged on a Nikon Ti Eclipse microscope with an Andor Ikon-M camera and a 60 \times /1.4NA Plan Apo λ objective with an additional 1.5 \times magnification.

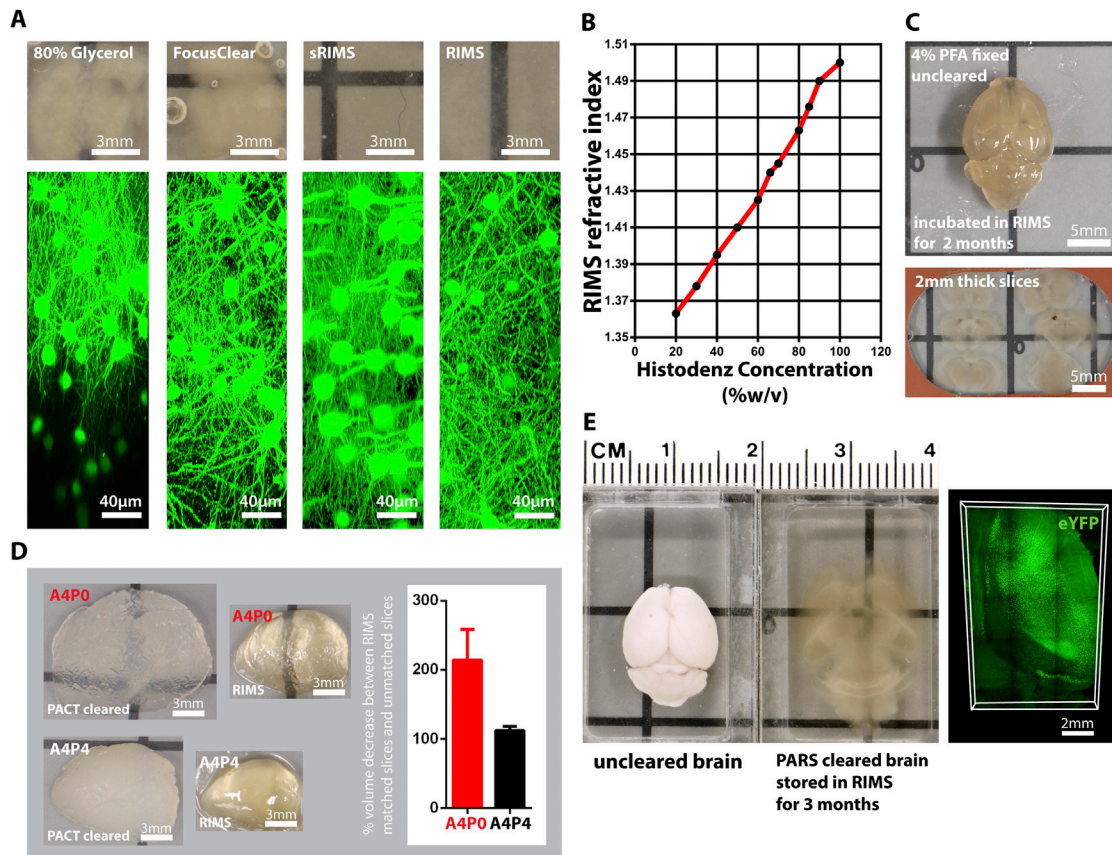


Figure S3. sRIMS and RIMS Give Better Optical Transparency by Matching the Refractive Index of Cleared Tissue-Hydrogel Hybrid and Allow for Long-Term Storage and Imaging, Related to Figures 1 and 4, and Table S2

(A) Optical transparency (top, bright field camera) and confocal images (bottom) of PACT cleared 1 mm Thy1-eYFP mouse brain coronal slices mounted and stored for 2 weeks in different media. Whereas the optical transparency of samples mounted in 80% glycerol was very poor, RIMS and sRIMS, a sorbitol solution-based mounting media (see [Extended Experimental Procedures](#)), enhanced the optical transparency and imaging resolution depth of mounted samples. We detected precipitation, perhaps of dissolved salts, in tissue that had been mounted in glycerol and FocusClear for more than 1 day.

(B) The refractive index of RIMS prepared with various concentrations of Histodenz (diluted in phosphate buffer).

(C) After a 2 month incubation in RIMS, uncleared whole-brain tissues become optically transparent in superficial, poorly myelinated regions. Thus, RIMS immersion offers a milder, albeit slower, alternative to more involved clearing protocols when superior resolution is desired for thick-sectioned (~50–300 μ m) tissue slices.

(D) Representative images (bright field camera) and the quantification of the percentage of tissue shrinkage of PACT cleared (3 days) 3 mm Thy1-eYFP mouse brain sagittal blocks after incubated in RIMS for 1 day ($n = 4$ blocks) for A4P0 and A4P4 hydrogel-tissue hybrids.

(E) A size comparison between uncleared Thy1-eYFP whole-brain and a PARS cleared Thy1-eYFP whole-brain mounted in RIMS for 3 months (bright field camera), and the eYFP fluorescence signal ($z = 1$ mm) after long-term storage in RI 1.42 (60% Histodenz w/v) RIMS.

Objectives used for confocal imaging: (A) LD LCI Plan-Apochromat 25 \times /0.8 Imm Corr DIC M27 multi-immersion objective; (E) Fluor 5 \times /0.25 M27 objective.

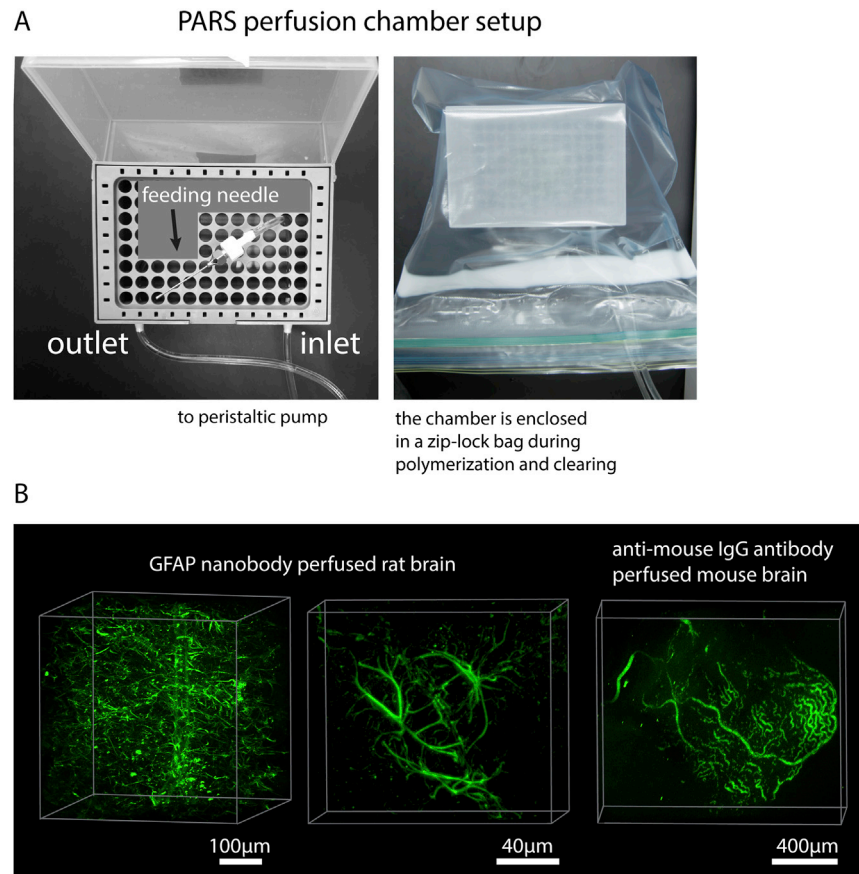


Figure S4. Development of PARS System for Whole-Body Clearing, Related to Figures 3 and 4

(A) Left: PARS was conducted in custom-built perfusion chambers prepared from pipette boxes. Following perfusion fixation with 4% PFA through a feeding needle that is affixed to the left ventricle or ascending aorta, the rodent is secured atop the pipette tip grating. To drain the pipette box as it fills with perfusate that exits the rodent body through a lesion in the right atrium, one end of a catheter tube is secured to the bottom of the pipette tip box. The tubing is then threaded through a peristaltic pump, and the opposite end is connected to the feeding needle. This allows perfusate to be siphoned out of the pipette box and recirculated back through the cardiac catheter, achieving continuous perfusion of hydrogel monomers, wash buffer, clearing detergents, and histological stains through the rodent vasculature. Of note, this PARS set-up may be applied to PARS-CSF (see Figure 3A) by attaching catheter tubing to the intracranial cannula rather than feeding needle. Right: Immediately prior to hydrogel polymerization, the entire perfusion chamber (with catheter-connected subject) is sealed within a ziplock bag for tissue degassing, and the entire set-up is left within this bag throughout the rest of the PARS protocol. The bag allows the perfusion chamber to be placed in a shallow water bath—forming a barrier to prevent water from flooding the perfusion chamber, or from PARS reagents from contaminating the water bath.

(B) Rodents were perfused with Atto 488-conjugated GFAP nanobody (left) and Alexa Fluor 647-conjugated anti-mouse IgG antibody (right) to investigate whole-body vasculature accessibility via the perfusion of PACT reagents. Specifically, PACT reagents must be able to circulate through both major blood vessels as well as tissue microvasculature in order to achieve uniform, rapid clearing and labeling of all tissues, poorly- or well-vascularized. Left: extensive populations of glial cells surrounding a major vessel in the cortex. Middle: high-magnification volume rendering showing astrocytic endfeet participating in the formation of the blood brain barrier. Right: well-preserved vasculature of a 1 mm mouse brain section (cortex) achieved via perfusion-based delivery of whole immunoglobulins into uncleared tissue. The extensive labeling of mouse vasculature suggests that the PARS pressure gradient can drive antibody solutions through major blood vessels. Also see Movie S1.

Objectives used for confocal imaging: (B, Left) LD LCI Plan-Apochromat 25×/0.8 Imm Corr DIC M27 multi-immersion objective; (B, Right) 10× 0.45 N.A. Plan-Apochromat.

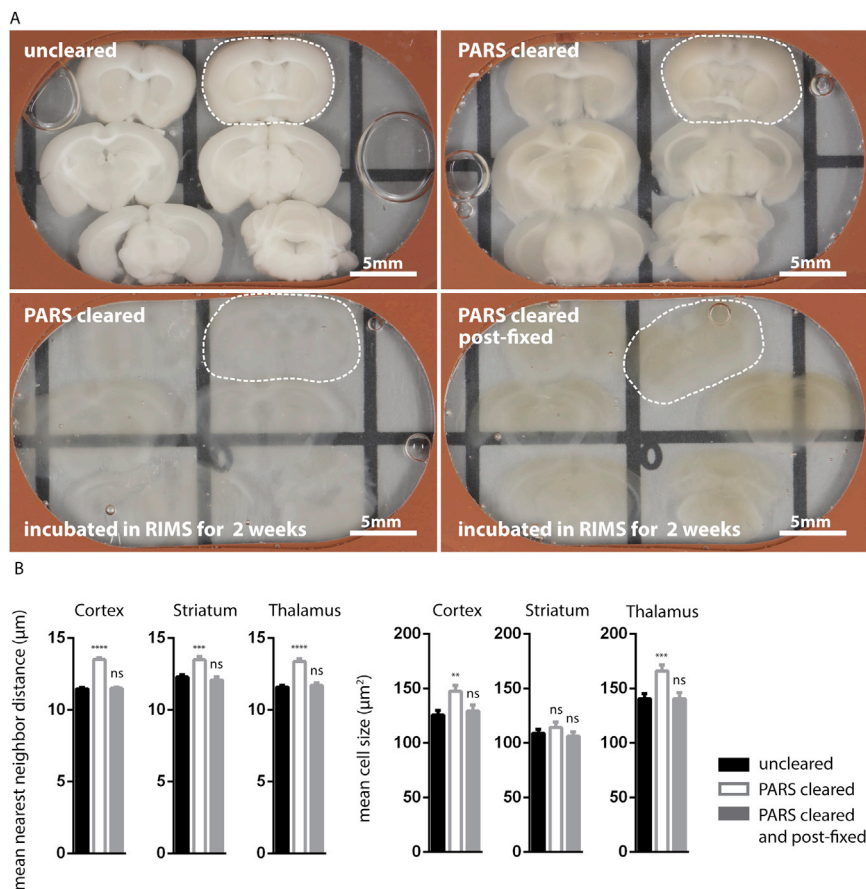


Figure S5. Tissue Preservation and Quantification, Related to Figures 4 and 5

(A) Bright field images of 1-mm-thick mouse brain slices from uncleared (top left), PARS-cleared (top right), PARS-cleared and 2 week RIMS immersion (bottom left), and PARS-cleared, 4% PFA postfixed and RIMS mounted mouse brain sections. Note the slices are from the whole brains in Figure 4C.

(B) The mean nearest neighbor distance between cells in the cortex, striatum and thalamus were quantified in uncleared, PARS-cleared, and PARS-cleared then postfixed brains slices. Compared to the uncleared control, PARS-cleared brain slices showed a small but significant increase in cell spacing (left, data presented as mean \pm SEM) in all three regions of the brain and significant increase in cell size (right, data presented as mean \pm SEM) in the cortex and thalamus while PARS-cleared then postfixed brain slices did not.

Statistical significance for multiple comparisons: one-way ANOVA (** $p < 0.01$, *** $p < 0.005$, **** $p < 0.0005$, ns = not significant).

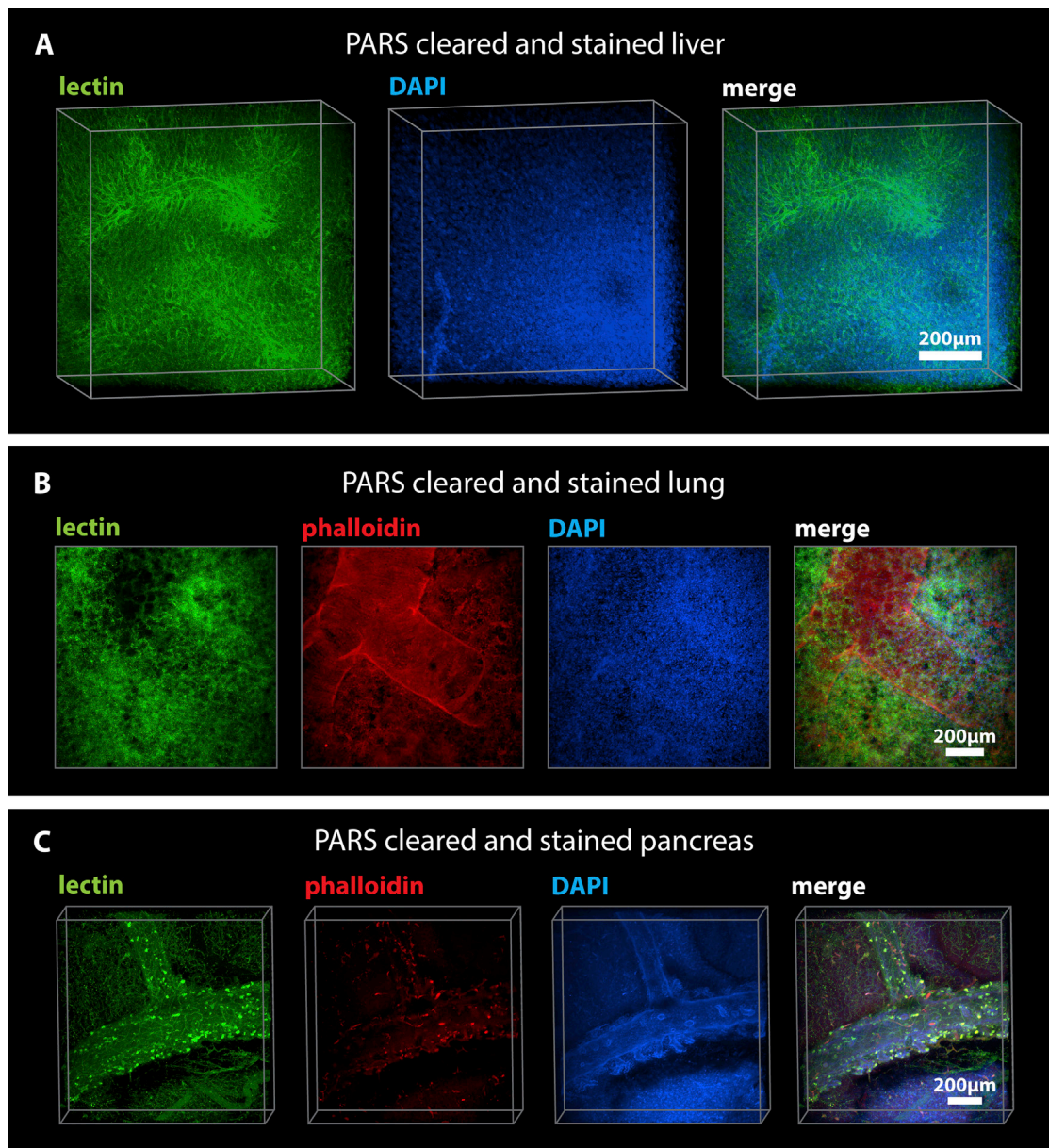


Figure S6. PARS Renders Major Organs Optically Transparent, Related to Figure 6

(A–C) Following 1 week of PARS clearing and perfusion-labeling, major organs were excised and immersed in RIMS for 24 hr before imaging. (A) 500 μ m imaging stack of PARS-cleared and stained mouse liver sample, with diffuse lectin and DAPI staining suggesting that PACT reagents were able to access dense tissue. (B) 100 μ m imaging stack of PARS-cleared and stained mouse lung sample and (C) 600- μ m-thick imaging stack of PARS-cleared mouse pancreas sample, both exhibiting high-level lectin, phalloidin and DAPI fluorescent signals throughout. We observed fine resolution of cellular structures in all three tissue samples. Lectin staining, which marks blood vessels, in combination with the fluorescent signals of other small-molecule dyes demonstrate that vascularized tissue can be effectively cleared and labeled with PARS. In major organs, immunolabeling occurs via both vasculature circulation and passive diffusion of perfusate through organs.

Objectives used for confocal imaging: 10 \times 0.45 N.A. Plan-Apochromat.

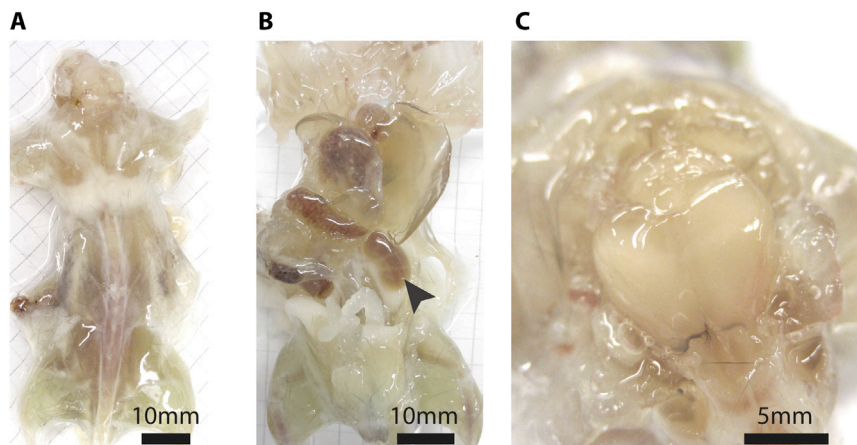


Figure S7. PARS Is Capable of Whole-Body Clearing, Related to Figure 4

(A and B) The (A) dorsal and (B) ventral view of whole Thy1-eYFP mouse after PARS clearing with 8% SDS for 1 week showed good optical transparency of whole body. Arrowhead in (B) points to cleared kidney. (C) The image of the brain for the same mouse. Images were taken using bright field camera.